BUFFET INVESTIGATION ON AIRFOILS

A THESIS SUBMITTED TO
THE GRADUATE SCHOOL OF NATURAL AND APPLIED SCIENCES
OF
MIDDLE EAST TECHNICAL UNIVERSITY

BY

KEZBAN GİZEM ALGÜL

IN PARTIAL FULFILLMENT OF THE REQUIREMENTS
FOR
THE DEGREE OF MASTER OF SCIENCE
IN
AEROSPACE ENGINEERING

APRIL 2021

Approval of the thesis:

BUFFET INVESTIGATION ON AIRFOILS

submitted by **KEZBAN GİZEM ALGÜL** in partial fulfillment of the requirements for the degree of **Master of Science** i**n Aerospace Engineering, Middle East Technical University** by,

Prof. Dr. Halil Kalıpçılar
Dean, Graduate School of **Natural and Applied Sciences** _____

Prof. Dr. İsmail Hakkı Tuncer
Head of the Department, **Aerospace Engineering** _____

Prof. Dr. Serkan Özgen
Supervisor, **Aerospace Engineering, METU** _____

Examining Committee Members:

Prof. Dr. Zafer Dursunkaya
Mechanical Engineering, METU _____

Prof. Dr. Serkan Özgen
Aerospace Engineering, METU _____

Prof. Dr. İsmail Hakkı Tuncer
Aerospace Engineering, METU _____

Prof. Dr. Yusuf Özyörük
Aerospace Engineering, METU _____

Prof. Dr. Kürşad Melih Güleren
Faculty of Aeronautics and Astronautics, ESTU _____

Date: 30.04.2021

I hereby declare that all information in this document has been obtained and presented in accordance with academic rules and ethical conduct. I also declare that, as required by these rules and conduct, I have fully cited and referenced all material and results that are not original to this work.

Name, Last name : Kezban Gizem Algül

Signature :

ABSTRACT

BUFFET INVESTIGATION ON AIRFOILS

Algül, Kezban Gizem
Master of Science, Aerospace Engineering
Supervisor: Prof. Dr. Serkan Özgen

April 2021, 108 pages

The aim of the present thesis is to investigate buffet onset characteristics in two-dimensional flow. NACA0012 airfoil was chosen as the geometry in this study since the profile is frequently used for the lifting surfaces of aircraft, which are exposed to high flight loads during transonic flight and this causes buffet and flutter. In addition, it is one of the very few models which was studied for the buffet onset investigation in the literature and detailed wind tunnel test data is available. In the present study, after determining the optimum mesh resolution and the appropriate turbulence model, the results of the steady flow numerical analysis for low and high Reynolds numbers were validated with wind tunnel data. The transient flow is investigated for the buffet onset region of the NACA0012 airfoil and the results are verified with wind tunnel data. The oscillating behavior of the shock wave on the airfoil is investigated through the frequency and the Strouhal numbers of lift, drag, moment and static pressure distributions through time and frequency.

The study investigates the primary effectors that stimulate buffet onset and the behavior of the flow during buffet through numerical analyses using Unsteady Reynolds-Averaged Navier-Stokes (U-RANS) Equations. The effects of Mach

number, angle of attack and Reynolds number on buffet onset is investigated for the examination of buffet characteristics in detail.

Keywords: Buffet, Buffet Onset, Shock Induced Oscillation, Unsteady Transient Flow Physics, Aeroelasticity

ÖZ

KANAT PROFİLLERİNDE BUFFET ARAŞTIRMASI

Algül, Kezban Gizem
Yüksek Lisans, Havacılık ve Uzay Mühendisliği
Tez Yöneticisi: Prof. Dr. Serkan Özgen

Nisan 2021, 108 sayfa

Bu tezin amacı, iki boyutlu akışta buffet başlangıç özelliklerini incelemektir. Bu çalışmada transonik uçuş sırasında yüksek uçuş yüklerine maruz kalan uçakların kaldırma yüzeylerinde sıklıkla kullanılması ve bu durumun buffet ve çırpınmaya neden olması sebebiyle geometri olarak NACA0012 kanat profili seçilmiştir. Ayrıca, literatürde buffet başlangıç araştırması için incelenen çok az sayıda modelden biridir ve detaylı rüzgar tüneli test verileri mevcuttur. Optimum ağ çözünürlüğü ve uygun türbülans modelinin belirlenmesi için öncelikle sabit akış analizleri yapılmıştır. Mevcut çalışmada, optimum ağ çözünürlüğü ve uygun türbülans modeli belirlendikten sonra, düşük ve yüksek Reynolds sayıları için sürekli akış sayısal analizlerinin sonuçları rüzgar tüneli verileri ile doğrulanmıştır. Zamana bağlı akış ise, NACA0012 kanat profilinin buffet başlangıç bölgesi için araştırılmış ve sayısal analizlerden elde edilen sonuçlar rüzgar tüneli verileri ile doğrulanmıştır. Şok dalgasının kanat üzerindeki salınım davranışı, kaldırma ve sürükleme kuvvetlerinin, yunuslama momentinin ve statik basıncın zamana ve frekansa göre dağılımlarından elde edilen güç spektral yoğunlukları ve Strouhal sayıları kullanılarak araştırılmıştır.

Çalışmada, buffet başlangıcını uyaran birincil efektörler ve buffet sırasındaki akış davranışı Reynolds-Ortalamalı Navier-Stokes denklemleri kullanılarak sayısal analizlerle araştırılmıştır. Buffet özelliklerinin detaylı incelenmesi için Mach sayısı, hücum açısı ve Reynolds sayısının buffet başlangıcına etkileri araştırılmıştır.

Anahtar Kelimeler: Buffet, Buffet Başlangıcı, Şok Kaynaklı Salınım, Zamana Bağlı Kararsız Akış Fiziği, Aeroelastisite

To my family

ACKNOWLEDGEMENTS

I would like to express my deepest gratitude to my supervisor Prof. Dr. Serkan Özgen for his guidance, advice, criticism, encouragement and insight throughout the research. I am grateful not only for his support by sharing his vast knowledge and by giving morale where I fell into despair throughout my thesis, but also the support that he gave me in my business life whenever I demanded help and guidance.

I would like to thank my friends, for their support, encouragement and help when I was struggling and got stuck during my thesis work.

I would like to express my deepest love and gratitude to my dear father Ali Parlak, my dear mother Gülsüm Parlak, my brother Mehmet Alper and my sister Mehtap Ayfer, for their endless, complimentary love and support throughout my thesis and most importantly throughout my whole life.

I would like to express my deepest love to my dear beloved husband, Kadir Algül for his endless support and love even in the most difficult times during thesis studies and most importantly during my whole life.

TABLE OF CONTENTS

LIST OF TABLES

TABLES

LIST OF FIGURES

FIGURES

LIST OF ABBREVIATIONS

ABBREVIATIONS

CFD	: Computational Fluid Dynamics
Hz	: Hertz
MTE	: Mean Turbulent Energy
MVF	: Mean Velocity Field
NLEVM	: Nonlinear Eddy Viscosity Models
PSD	: Power Spectral Density
RANS	: Reynolds Averaged Navier-Stokes Equations
SST	: Shear Stress Transport
U-RANS	: Unsteady Reynolds-Averaged Navier-Stokes Equations

LIST OF SYMBOLS

SYMBOLS

a	: Speed of Sound (m/s)
k	: Turbulent Kinetic Energy (J/kg)
K	: Thousands (x1000)
l_{ref}	: Reference Length (m)
M	: Mach number
p	: Pressure (Pa)
R	: Gas Constant ($JK^{-1}mol^{-1}$)
Re	: Reynolds Number
St	: Strouhal Number
t	: Timestep (sec)
T	: Period of Oscillation (sec)
T	: Temperature (K)
u	: Flow Velocity Components (m/s)
V	: Freestream Velocity (m/s)
y+	: Dimensionless Wall Distance

GREEK SYMBOLS

α	: Angle of Attack (°)
β	: Sideslip Angle (°)
ε	: Turbulence Dissipation Rate (m^2/s^3)
μ_t	: Turbulent Viscosity (Pa s)
ρ	: Density (kg/m^3)
τ_{ij}	: Stress Tensor
ω	: Turbulence Specific Dissipation Rate (1/s)

CHAPTER 1

INTRODUCTION

1.1 General Overview

Transonic buffet is defined as the shock induced oscillations that interact with turbulent boundary layer and cause separation especially in the region close to the trailing edge of the wing/airfoil [1]. The instabilities in the flow field interacting with turbulent boundary layer cause oscillations in the shock wave. The critical flow variables that trigger transonic buffet are Mach number and angle of attack. These two parameters construct the buffet onset region, in which the critical flight conditions that cause the buffet phenomenon are stated. The relation of the critical Mach number and angle of attack that cause buffet onset is actually inversely proportional. The critical maximum angle of attack that stimulates the buffet decreases when the critical Mach number increases. As it is seen on Figure 1.1, the resultant curve separates the stability behavior of the flow field around the airfoil into two regions as steady and unsteady flow. The flow conditions that are on the lower region of the buffet onset represents the steady flow and no such characteristics as oscillating shocks are observed in that region. When the flow conditions are reached on and above the buffet onset, the unsteady flow starts to be observed and the shock oscillations can be observed in that region.

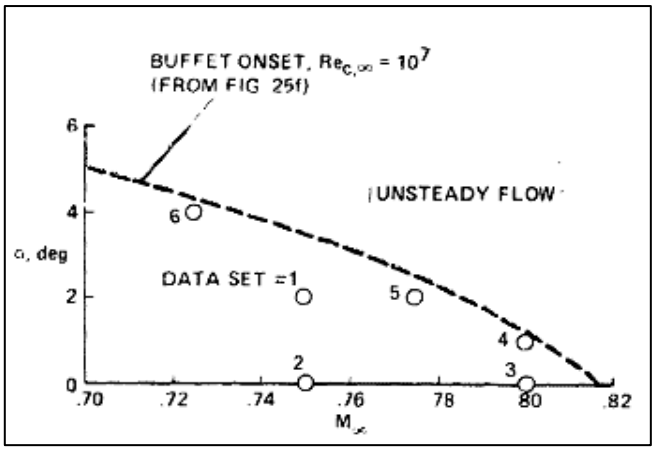

Figure 1.1. Buffet Onset of NACA0012 Airfoil [2]

In addition to the critical flow conditions that trigger buffet, the Reynolds number is an important parameter to define the characteristics and frequency of the oscillations occurring on the profile. The observations on the buffet physics reveal that, the buffet frequency increases with the increase in Reynolds number with constant Mach number and angle of attack [2]. Especially at high Reynolds numbers, the oscillations on the flow reach to maximum level, and the buffet frequency increases dependently. Considering all of these effects, the buffet phenomenon can be investigated based on the effects of Mach number, angle of attack and Reynolds number.

Buffet phenomenon occurring on airfoils can lead to several detrimental consequences on aircraft performance, stability & control characteristics and maintainability. Since the oscillating shock behavior causes strong separation on the rearward region of the airfoil, the buffet results in the reduction on the lift and increase in drag. Due to the reduction of the lift during flight and maneuvers can cause serious decreases in the performance. Buffet also has harmful effects on the structural strength of the aircraft. The oscillating shock with certain bandwidth causes the loads on the wing to act on the same area with similar oscillations for the duration that the buffet is observed. The oscillating loads on the wing lead to structural damage and even destruction especially when these oscillations are coupled with the natural frequency of the wing, which is also known as flutter.

Besides, transonic buffet occurs in transonic Mach numbers with critical angles of attack of small magnitude. For that reason, the aircraft flies in that region very frequently. Due to all of these reasons, the determination of the buffet onset of the configuration is crucially important for the aircraft. The investigations on the buffet onset is conducted for several planforms, and the current results are mainly focused on the airfoil and wing buffet characteristics. In this aim, the transonic buffet is investigated in two-dimensional environment.

1.2 The Motivation and Outline of the Thesis

The aim of the study is to obtain the transonic buffet onset characteristics of the NACA0012 airfoil with the Computational Fluid Dynamics using the commercial solver ANSYS Fluent. The results from the numerical solutions are compared with wind tunnel test results in the literature [2].

For this purpose, the steady analyses of the NACA0012 airfoil is conducted first. The three independent points as Dataset 4, Dataset 5 and Dataset 6 in Figure 1.1 are investigated and the characteristics of the flow at these points are examined for the investigation of the buffet onset characteristics of NACA0012 airfoil. The transonic buffet conditions are mainly determined by the critical Mach number and angle of attack conditions and these variables create buffet onset curve. The line at the buffet onset curve divides the flow characteristics of the NACA0012 airfoil into two region as steady and unsteady flow characteristics, and the thesis includes the assessment of both regions in terms of flow behavior. At this phase, the mesh quality, independence from the resolution and turbulence models are investigated and validated with the wind tunnel data. The verification of the numerical solutions is conducted for two different Reynolds number conditions for the steady flow. Then, the transient flow analyses are conducted for both steady and unsteady regions. The steady analyses are conducted at the Dataset 4, Dataset 5 and Dataset 6 flow

conditions. The unsteady flow is analyzed by adding approximately 2 degrees of angle of attack and keeping Mach number constant in Dataset 4, Dataset 5 and Dataset 6 flow conditions. In this way, the characteristics of the flow can be observed in the steady region, and the change can be better observed when going through the unstable region after buffet onset. The transition from steady to unsteady flow is conducted by increasing the angle of attack when the Mach number is kept the same. Then, the validation of the buffet onset for the unsteady transonic flow is carried out with high Reynolds number.

The study of the buffet onset starts with the steady analyses. The pressure distribution around airfoil is investigated at stable region of the buffet onset curve at Figure 1.1, and then the results are verified with the wind tunnel data [2]. The second phase of the study includes the transient analyses. Firstly, variance in the flow characteristics with time is examined in the steady region of buffet onset, and then the same examination is conducted for the unstable region. Finally, the buffet characteristics of the NACA0012 airfoil is verified with wind tunnel data at high Reynolds number [2].

CHAPTER 2

LITERATURE REVIEW

The buffet onset investigations are generally carried out in experimental studies and numerical analyses. The experimental studies are conducted for several airfoil types and the measurements and analyses of the data are published. The numerical analyses are based on the Computational Fluid Dynamics results with several types of tools and sources. The results of the numerical analyses are compared with experimental studies so as to be verified with physical data.

Even though Hilton & Fowler [3] performed experiments on transonic shock induced oscillations sixty years ago, the physical mechanisms behind them still could not be fully understood. By various experiments and numerical analysis, two different types of shock buffet on airfoils have been identified. The first type of buffet includes shock oscillations on both the pressure and suction surfaces of an airfoil, which typically occur at zero incidence on biconvex sections. Mabey [4] investigated a model of the first type shock buffet where shock wave/boundary layer interactions on both surfaces initiate phaselocked shock oscillations in opposing directions. The shock moving upstream on the upper surface weakens so that the separated zone becomes reattached and this propels the shock downstream. The first type buffet is strongly dependent on the shock which can produce separation. Mabey suggested the prediction for buffet onset with the Mach number just ahead of the shock [4] .

The second type of the buffet is common in modern supercritical airfoils and is characterized by the shock oscillations on the upper surface of the airfoil at angles of attack which are different than zero. Pearcey [5], [6] characterized the shock induced separation forms, which are defined as the separation bubbles on the upper surfaces, experienced by conventional airfoils at transonic speed. He identified two

different types of separation; shock induced separation bubble and rear separation, which is either additionally present or in its initial state. Also three variants of rear separation were identified; first rear separation is provoked by the formation of a bubble, second is provoked by the shock and the third is present from the outset.

Research by Pearcey et al led to the creation of the first model to initiate predictions of the shock oscillations that are observed on supercritical airfoils. The model makes a relation between trailing edge pressure divergence and large scale unsteadiness. For airfoils that contain separation bubbles, Pearcey et al [6] associate the onset of buffets with the Mach number or angle of attack at which the separation bubble expands to the trailing edge and bursts. This mechanism of bubble bursting leading to buffet onset is identified by the divergence of trailing edge pressure. At first, bubble bursting was thought as the cause of onset by experimental and computational support, however conflicting evidence are found during latest research [7], which discounts the bubble bursting as a potential leading factor for shock buffet.

In the advanced work of Tijdeman [8], three different modes of shock motion with the effect of sinusoidal flap deflections were experimentally demonstrated on the NACA 64A006 airfoil. Shock movement of the first type is represented near sinusoidal shock oscillations on the upper surface of the airfoil, for which the shock is present throughout the entire buffet cycle, but varies in strength, while the maximum shock strength is achieved during the upstream excursion. The magnitude of the difference in shock strength is quite large in the second type when compared to the first type, and as a result the shock disappears during the downstream excursion. The behavior in the third type is quite different from the others. The shock moves upstream, at first strong and then weakening, but continues to move, eventually moving onto the oncoming flow as a free shock wave. Although these shock wave motions were initially identified with oscillating airfoils, observations in rigid wing sections at certain flight conditions have been performed for each of them [9].

For the Tijdeman's first type of shock movements [8], an acoustic wave-propagation feedback model is proposed by Lee [1] explaining the mechanism governing the

autonomous shock oscillations. According to this model, the shock wave motion generates downstream propagating pressure waves, with the instability growing as it travels from the separation point through the shear layer. The separated flow induces a de-cambering effect, because of the interactions with the flow on reaching the trailing edge, upstream moving pressure waves are produced in the subsonic flow above the boundary layer. These waves interact with the shock and impart energy to maintain its oscillation. The loop is then completed resulting in sustained shock motion. There is conflicting evidence in the literature regarding the validity of the Lee model [1], according to Pearcey bubble bursting mechanism [6].

Raghunathan et al [10] also proposed a mechanism based on an instable interaction between shock wave and separation bubble like Tijdeman's second type shock oscillations on the NACA0012 airfoil [8]. Shock strength sufficiency for inducing a separation bubble is highlighted by the authors which initiates periodic motion of the shock. This motion is sustained on the upper airfoil surface by the alternating expansion and collapse of the bubble. Throughout the cycle, the varying size of the separated zone changes the effective curvature of the airfoil and the trailing edge plays an integral role in the communication of flow states between the suction and pressure surfaces.

The phenomenon of transonic shock buffet described until now reflects a classical perspective, including most of the early experimental and numerical investigations which tries to model the underlying flow mechanisms. An overall review of these works is provided by Lee [9].

2.1 Experimental Studies

There are several distinctive experimental studies addressing buffet investigation. One of these is Tijdemann's work [8], which examined the NACA64A006 airfoil with several flap movements and deflections during the experiments. By this way, the work is intended to study the effect of sinusoidal flap behavior on the airfoil

profile. Each of the writers McDevitt et al [11], McDevitt [12], Mabey [4] tested a biconvex airfoil in wind tunnel. Tests taking into account shock oscillations in supercritical airfoils were performed by Lee [13], [14].

McDevitt & Okuno [2] reviewed NACA0012 buffet on NASA Ames High Reynolds number facility. The chord of the model was 20.32 cm; the trailing edge thickness was 0.002c. The tests were conducted for the Mach numbers that are ranging from 0.7 to 0.8, and the Reynolds numbers that are ranging from 1 million to 14 million. The static pressure measurements are conducted from the 40 static pressure orifices that are placed on the airfoil surface, and the unsteady behavior of the flow is characterized by the measurements from the 6 dynamic pressure transducers. Schlieren images were also added to the work in order to reflect the visual behavior of the flow field during buffet. The authors examined not only the factors that affect the buffet onset, but also the Reynolds number effect on the buffet characteristics. The Strouhal number values of the shock oscillations during the buffet are measured from the experimental results with high Reynolds number.

Dandois et al give detailed information about the experimental tests in ONERA about examining and reducing the possible effects of the buffet phenomenon in his works [15]. Especially, the tests of the supercritical OAT15A airfoil conducted in the S3Ch continuous investigation wind tunnel at the ONERA Chalais-Meudon-Center have been described by Jacquin et al [16], [17].

In order to obtain a wide range of experimental database for the verification of the numerical results, the tests were conducted with varying test conditions and results. In this manner, in addition to the surface static and dynamic pressure measurements, mean and RMS pressure data with spectral content for pressure fluctuations were produced.

Tests performed by Jacquin et al [16] include varying angles of attack with constant Mach number as M = 0.73, varying Mach numbers with constant angles of attack as $\alpha = 3°$ and $\alpha = 3.5°$ and constant Reynolds number as $Re \approx 3x10^6$ for all test conditions. OAT15A has become the benchmark for transonic buffet test case in recent years

according to the measurements of the tests and the numerical studies that are conducted in the same conditions of the tests for this category [18], [19], [20], [21].

The detailed analysis by Jacquin et al [16] also provided new insights into the physics of transonic shock oscillations. Spectral analysis of unsteady pressure signals reveals that a two-dimensional buffet phenomenon is time-invariant and mostly modal in nature. The spectra are monitored by a single frequency, excluding the fact that the frequency propagation is caused by low frequency shock wave oscillations. This behavior confirms the global instability theory proposed by Crouch et al [22].

In a study of the two-dimensional characteristics of the buffet, somehow conflicting results have been observed. Jacquin et al [16] firstly observed that the spectral density of the sound pressure level in the central span distributes evenly and this is the evidence of a two dimensional buffet mechanism occurring on the airfoil. Yet, the three dimensional effects have been realized in the oil flow visualizations. At this point, the values and the order of magnitudes of the measurements from the pressure taps and the oil flow visualizations should be taken into account. The study revealed that the pressure occurs from the Euler flow around viscous layers and the order of magnitude is equivalent to the dynamic pressure. On the other hand, the oil flow visualizations reveal the wall velocity field and the order of magnitude is obviously less than that of dynamic pressure. As a result, although three dimensional characteristics have been observed in the oil flow, since the order of magnitude is significantly small compared to the two dimensional buffet characteristics, this effect is considered as a weak impact and it should be investigated in detail. Thus, Jacquin et al [16] conclude that the buffet instability may be the result of a combination of strong two-dimensional and weaker three-dimensional global modes.

Jacquin et al [16] also agree with Lee's argument [1] that the buffet period observed for airfoils was the sum of the disturbance convection time scales. Additional timescales include the amount of disturbance time that emerges at the shock foot and proceeded to the trailing edge and an acoustic time delay between the perturbations that come from the trailing edge and hit to the shock. The authors note that the absence of a global physics that conducts the buffet phenomenon in a general

empirical model poses a number of difficulties, especially in measuring the corresponding convection velocities.

While Lee [1] assumes that acoustic time delay is the time spent for acoustic waves transferred upstream over the upper surface of the airfoil from the trailing edge, Jacquin et al [16] claims that this kind of disturbances can move toward the shock along the lower surface, turn around leading edge and cause shock from upstream.

Jacquin et al [16] mentioned the problems of accuracy in calculating the convection velocity while computing disturbance time. The authors use a two-point cross-correlation of the pressure fluctuations for calculating convection velocity, with velocities similar to the values obtained by Lee [1]. The observation of the perturbations affects the values of the convective speeds taking into account the local stability theory and were characterized by an increase in the Kelvin-Helmholtz type instability. Kelvin-Helmholtz type instability occurs on the higher band of frequency or Strouhal numbers than buffet instability as seen in Figure 2.1, and it originates from the shear layer between separation downstream of the shock wave and the outer flow [23].

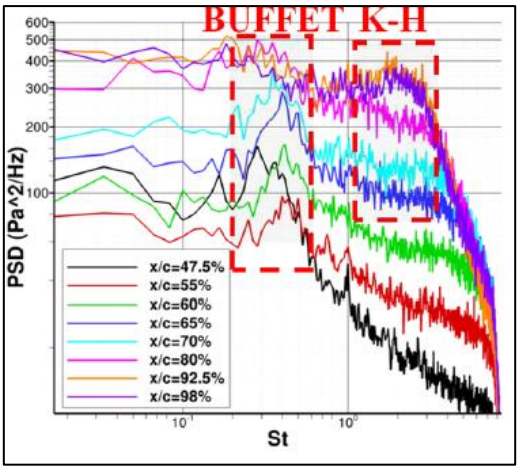

Figure 2.1. Sample of Kelvin-Helmholtz Type Instability on PSD of Pressure from Different Chordwise Locations, OAT15A Airfoil [23]

While the modified multiplication model better reflects the flow characteristics observed in the experiments, the authors united into a common decision that a simple and robust model is not able to fully reflect the characteristics of the flow. Shock oscillations are caused by two modes of interaction; propagation of the disturbances that arise from sensitive region of the shock foot and the propagation of these disturbances through the convection of acoustic waves. A generalized common model cannot be constructed due to the complex mechanisms of the constituent flow according to the judgements of the authors.

2.2 Numerical Studies

In order to reflect the characteristics of the buffet phenomenon, several numerical studies were conducted for examining the efficiency of U-RANS models [24], [25]. Moreover, several authors have reported good correlations for investigating buffet characteristics with a Reynolds-averaged formulation [26]. The low frequency shock of the transonic buffet explains the success of the U-RANS approach. Crouch et al [7] have noted that global instability occurs in longer timescales than the characteristic eddy timescales, at which mostly turbulent viscous shear layer flow is seen on high Reynolds numbers. Thus, the fundamental buffet characteristics can be predicted with high accuracy with U-RANS simulations. The representation of complex characteristics of the buffet phenomenon involving turbulence with varying scales with U-RANS simulations is highly dependent on the turbulence model, spatial and temporal discretization, and the numerical scheme used.

The U-RANS models of the shock buffet phenomenon is especially affected by the turbulence model. Barakos & Drikakis [27] studied the efficiency of various linear and nonlinear eddy viscosity models (NLEVM) using a nonlinear regenerative solution of Riemann solver of the third order spatial and second order temporal accuracy [28]. The authors applied the experiments of McDevitt and Okuno [2] to evaluate the performance of Baldwin-Lomax [29], Spalart-Allmaras [30], Launder-

Sharma [31] and Nagano-Kim [32] linear k-ε model and Sofialidis-Prinos k-ω version [33] of the Craft-et al [34] nonlinear eddy-viscosity model for capturing transonic shock oscillations on the NACA0012 airfoil. The results show that for high angle of attack and Mach number conditions, Spalart-Allmaras and NLEVM models can only give acceptable behavior of unsteady flow due to shock oscillation when compared to the experimental results.

Baracos and Drikakis [27] stated that the k-ω model is not a very successful turbulence model for reflecting unsteadiness for the buffet onset at low levels. In addition, introducing a realizability correction to the model significantly improves the behavior. The Spalart-Allmaras model can only predict the unsteady flow behavior over the well-known frequency and amplitude characteristics of the buffet. The Kok k-ω exhibits unsteady flow, although the onset of the oscillation is delayed to a higher angle of attack. Wilcox and Menter's k-ω models cannot reproduce shock oscillation without SST correction.

Kourta et al [35] found a time-dependent k-ε model [36] in which the model coefficient C_μ is related to local levels of deformation and strain stress, which is well achieved by calculating buffet on the OAT15A airfoil.

Xiao et al [37] have revealed that the lagged k-ω model of Olsen & Coakley [38] showed a good prediction of the airfoil pressure distribution of BGK No. 1 airfoil in buffet, but the magnitude of the oscillations is highly overestimated at the shock wave. Carresse et al [39] and Giannelis & Vio [40] also discovered that the SST model works significantly well with OAT15A airfoil.

CHAPTER 3

COMPUTATIONAL SOLUTION METHOD

Turbulence modeling is defined as computation of the turbulent flow using partial differential equations [41]. The resultant approaches of turbulence modeling are applicable for the Navier-Stokes equations. The flow variables are split into averaged and unstable parts in the first place for the approach in the Reynolds Averaged Navier-Stokes (RANS) equations. The stress tensor parameter is obtained by addition of the Reynolds variables into the equation.

3.1 Navier-Stokes Equations for Compressible Flow

3.1.1 Continuity Equation

The continuity equation defines the conservation of mass of a moving fluid. The change in density is obtained from the masses entering and leaving per unit time [42]. The equation can be stated in tensor notation.

$$\frac{\partial \rho}{\partial t} + \frac{\partial}{\partial x_i}(\rho u_i) = 0 \tag{3.1}$$

ρ represents the gas density and u_i are the flow velocity components.

3.1.2 Momentum Equation

Momentum equation states the motion of the gas flow according to Newton's Second Law of Motion. The summation of the external forces acting on the body gives the

product of the mass and acceleration [42] as it is represented using tensor notation below:

$$\frac{\partial}{\partial t}(\rho u_i) + \frac{\partial}{\partial x_j}\left(\rho u_i u_j + p\delta_{ij} - \tau_{ij}\right) = \rho f_i \qquad (3.2)$$

p is the gas pressure and τ is stress tensor, while $f_i$represents the acceleration of the gas due to the body forces.

3.1.3 Energy Equation

The first law of thermodynamics is applied to the motion of the gas in order to obtain the rate of change of the total energy of the gas with time in the equation. The energy equation can be stated in tensor notation.

$$\frac{\partial}{\partial t}(\rho E) + \frac{\partial}{\partial x_i}\left[\rho u_{ij}\left(E + \frac{p}{\rho}\right) - r_{ij}u_{ij} + q_i\right] = \rho f_i u_i \qquad (3.3)$$

The total specific energy of gas is represented as E and the heat flux leaving the gas as q in the equation. The total specific energy consists of the internal and kinetic energies.

$$E = e + \frac{U^2}{2} \qquad (3.4)$$

3.1.4 Thermodynamic Relation

For the thermodynamics relation through the fluid flow, the gas is considered as ideal gas. The pressure, p is related to the density ρ and temperature T of the ideal gas.

$$p = \rho RT \qquad (3.5)$$

The specific energy can be obtained in relation with temperature and specific heat at constant volume, c_v for ideal gas. In a similar relation, the total specific energy can be obtained by the relation of temperature and specific heat at constant pressure, c_p for ideal gas.

$$e = c_v T = \frac{p}{(\gamma - 1)\,\rho} \tag{3.6}$$

and,

$$h = e + \frac{p}{\rho} = c_p T = \frac{\gamma p}{(\gamma - 1)\rho} \tag{3.7}$$

where γ is the ratio of specific heats defined as

$$\gamma = \frac{C_p}{C_v} \tag{3.8}$$

3.1.5 Mach Number and Speed of Sound

The speed of sound for ideal gas is related to the heat capacity ratio γ and temperature.

$$a = \sqrt{\gamma \frac{\mathrm{p}}{\rho}} = \sqrt{\gamma \mathrm{RT}} \tag{3.9}$$

Mach number is basically division of the flow speed by speed of sound.

$$M = \frac{u}{a} = \frac{u}{\sqrt{\gamma \mathrm{RT}}} \tag{3.10}$$

3.1.6 Reynolds Number and Strouhal Number

The Reynolds number is basically defined as the ratio between inertia forces to the viscous forces.

$$Re = \frac{\rho u l_{ref}}{\mu} \tag{3.11}$$

Where μ represents the dynamic viscosity. The Reynolds number is used for the determination of the flow transition from laminar to turbulent [42].

On the other hand, for the separation and vortex formation, the dimensionless frequency as Strouhal number is defined.

$$St = \frac{2\pi f l_{ref}}{u} \tag{3.12}$$

Where f is defined as the frequency of the vortex shedding. Strouhal number is used for the determination of the characteristics of the buffet phenomenon on airfoils and wings. It is a discriminative parameter for the identification of the buffet onset on airfoil.

3.2 Reynolds Averaged Navier-Stokes (RANS) Equations

Reynolds Averaged Navier-Stokes equations are obtained as the implementation of the Reynolds time average to the incompressible form of the Navier-Stokes equations. The additional terms due to time average in the continuity equation is stated in Eq. (3.13).

$$\overline{\frac{\partial u_i}{\partial t} + u_j \frac{\partial u_i}{\partial t} + \frac{1}{\rho}\frac{\partial p}{\partial x_i}} = \overline{\frac{\partial u_i}{\partial t}} + \overline{u_j \frac{\partial u_i}{\partial x_j}} + \overline{\frac{1}{\rho}\frac{\partial p}{\partial x_i}} = \overline{\frac{1}{\rho}\frac{\partial \tau_{ij}}{\partial x_j}} \tag{3.13}$$

Each term that is averaged over time can be expressed with index.

$$\overline{\frac{\partial u_i}{\partial t}} = \frac{\partial U_i}{\partial t} \tag{3.14}$$

$$\overline{\frac{1}{\rho}\frac{\partial p}{\partial x_i}} = \frac{1}{\rho}\overline{\frac{\partial p}{\partial x_i}} = \frac{1}{\rho}\frac{\partial P}{\partial x_i} \tag{3.15}$$

$$\overline{\frac{1}{\rho}\frac{\partial \tau_{ij}}{\partial x_j}} = \frac{1}{\rho}\overline{\frac{\partial \tau_{ij}}{\partial x_j}} = \frac{2}{\rho}\rho v\,\overline{\frac{\partial S_{ij}}{\partial x_j}} = 2v\,\frac{\partial \overline{S_{ij}}}{\partial x_j} \tag{3.16}$$

$$\overline{S_{ij}} = \frac{1}{2}\left[\frac{\partial U_i}{\partial x_j} + \frac{\partial U_j}{\partial x_j}\right] \tag{3.17}$$

Where $\overline{S_{ij}}$ represents the time average of stress.

$$\begin{aligned}
\overline{u_j\frac{\partial u_i}{\partial x_j}} = \overline{\frac{\partial}{\partial x_j}(u_i u_j)} - \overline{u_i\frac{\partial u_j}{\partial x_j}} &= \frac{\partial}{\partial x_j}\left(U_i U_j\right) + \overline{u_i' u_j'} \\
&= \frac{\partial}{\partial x_j}\left(U_i U_j\right) + \frac{\partial}{\partial x_j}\left(\overline{u_i' u_j'}\right) \\
&= U_j\frac{\partial U_i}{\partial x_j} + U_i\frac{\partial U_j}{\partial x_j} + \frac{\partial}{\partial x_j}\left(\overline{u_i' u_j'}\right) \\
&= U_j\frac{\partial U_i}{\partial x_j} + \frac{\partial}{\partial x_j}\left(\overline{u_i' u_j'}\right)
\end{aligned} \tag{3.18}$$

Finally,

$$\frac{\partial U_i}{\partial t} + U_j\frac{\partial U_i}{\partial x_j} + \frac{1}{\rho}\frac{\partial P}{\partial x_i} = \frac{1}{\rho}\frac{\partial}{\partial x_j}\left(2\mu\overline{S_{ij}} - \rho\overline{u_i' u_j'}\right) \tag{3.19}$$

The amount of averaged flow is defined from U_i and P.

$$\frac{\partial U_i}{\partial x_j} = 0 \tag{3.20}$$

$$\frac{\partial U_i}{\partial t} + U_j \frac{\partial U_i}{\partial x_j} + \frac{1}{\rho}\frac{\partial P}{\partial x_i} = \frac{1}{\rho}\frac{\partial}{\partial x_j}\left(\overline{\tau_{ij}} - \lambda_{ij}\right) \tag{3.21}$$

$\overline{\tau_{ij}}$ symbolizes the stress tensor of the fluid in terms of average flow amount and λ_{ij} symbolizes the eddy stress tensor.

$$\lambda_{ij} = \rho\overline{u_i' u_j'} \tag{3.22}$$

The RANS equations for the compressible flow is stated as in the following equations as the final form.

$$\frac{\partial \bar{\rho}}{\partial t} + \frac{\partial}{\partial x_j}\left(\bar{\rho} u_j\right) = 0 \tag{3.23}$$

$$\frac{\partial \bar{\rho} u_i}{\partial t} + \frac{\partial}{\partial x_j}\left(u_j \bar{\rho} u_j\right) = -\frac{\partial P}{\partial x_i} + \frac{\partial \overline{\sigma_{ij}}}{\partial x_j} + \frac{\partial \tau_{ij}}{\partial x_j} \tag{3.24}$$

$$\begin{aligned} &\frac{\partial \bar{\rho} e}{\partial t} + \frac{\partial}{\partial x_j}\left(u_j \bar{\rho} h\right) = \frac{\partial}{\partial x_j}\left(\overline{\sigma_{ij}} u_i + \overline{\sigma_{ij} u_i''}\right) \\ &-\frac{\partial}{\partial x_j}\left(\overline{q_j} + c_p \overline{\rho u_j'' T''} - u_i \tau_{ij} + \frac{1}{2}\overline{\rho u_i'' u_i'' u_j''}\right) \end{aligned} \tag{3.25}$$

The energy equation includes the viscous stress tensor and the approximation of the term for the compressible fluid with the Stoke's hypothesis [42] and can be stated as in Eq. (3.26).

$$\overline{\sigma_{ij}} \sim 2\mu\left(S_{ij} - \frac{1}{3}\frac{\partial u_k}{\partial x_k}\delta_{ij}\right) \tag{3.26}$$

From the assumption of

$$\lambda = -\frac{2}{3}\mu \tag{3.27}$$

3.3 RANS Equations Turbulence Models

RANS turbulence models are divided into 4 different classes. The classification is mainly constructed based on the equation number that is used on the model and the convection relation.

i. Zero Equation Model: Mean Velocity Field MVF Model is developed by Mellor and Herring [43]. There are four main models which represent Mean Velocity Field.
   a. Eddy-Viscosity Model for Reynolds Stress Tensor
   b. Vortex Model with Zero Equations
   c. Eddy-Viscosity Form
      i. Cebeci-Smith Model
      ii. Baldwin-Lomax Model
   d. Half Equation Model

ii. One Equation Model: The velocity ratio is calculated by taking into account the transport equation in this model, apart from Zero Equation Model. There are four main models which represent One Equation Model.
   a. Full Kinetic Energy Transport Equation
   b. Modeled Kinetic Energy Transport Equation
   c. One Equation Vortex Model
   d. Modeled Eddy-Viscosity Transport Equation
   e. Spalart-Allmaras Model

iii. Two Equation Model: Calculation of the turbulence length ratio by taking into account the convection equation is added as the second equation to the Single Equation Model. One and Two Equation Models are also called Mean Turbulent Energy (MTE) Models. There are seven main models which represent Two Equation Model.
   a. Kinetic Energy Transport Equation
   b. Full Diffusion-Rational Transport Equation

c. Modeled Diffusion-Rational Transport Equation
d. k-ε Model
e. k-kL Model
f. k-ω Model
g. Irregular Eddy-Viscosity Model

iv. Stress Equation Model: The model is obtained through adding convection equations as Reynolds stress tensor (τ_{ij}) and scalar propagation rate ($\tau_{ij} - \varepsilon$) to the Zero Equation Model. There are seven main models which represent Stress Equation Model.
a. Diffusion-Rational Transport Equation
b. Full Reynolds-Stress Transport Equation
c. Pressure Detached Correlation
d. Diffusion-Rational Correlation
e. Diffusion Correlation
f. Stress-Equation Vortex Model
g. Irregular Pressure-Stress Correlation Model

In order to obtain the most applicable representation of the turbulent flow around buffet onset on airfoil, three different types of turbulence models were used in this study. Spalart-Allmaras, k-ω SST and k-ε models are used and the comparative results are stated for the most suitable solution.

3.3.1 Spalart-Allmaras Turbulence Model

The Spalart-Allmaras model is a one-equation model that has a single transport equation for eddy viscosity. The implementation of the model in aerodynamics gives satisfactory results, especially for wall limited flows and reverse flows.

The boundary layer flows with a pressure gradient is the main design point of the model. The Spalart-Allmaras model is generally effective at low Reynolds numbers where viscosity affects the boundary layer (y +~1 solution networks).

The transformation of the Spalart-Allmaras turbulence model can be obtained by using a viscosity-like variable $\tilde{v}$, and it is the same as turbulent kinematic viscosity except for the wall edge region.

$$\frac{\partial}{\partial t}(\rho\tilde{v}) + \frac{\partial}{\partial x_i}(\rho\tilde{v}u_i) = G_v + \frac{1}{\sigma_{\tilde{v}}}\left[\frac{\partial}{\partial x_i}\left\{(\mu + \rho\tilde{v})\frac{\partial\tilde{v}}{\partial x_j}\right\} + C_{b2}\rho\left(\frac{\partial\tilde{v}}{\partial x_j}\right)^2\right] - Y_v + S_{\tilde{v}} \tag{3.28}$$

G_v represents the product of turbulent viscosities.

$$G_v = \frac{C_{b1}}{\kappa^2}C_{t3}\exp\left(-C_{t4}\left(\frac{\tilde{v}}{v}\right)^2\right)\rho\left(\frac{\tilde{v}}{y}\right)^2 \tag{3.29}$$

Y_v represents turbulent viscosity breakdown in the wall edge region due to wall interference and viscous damping.

$$Y_v = \left(\frac{C_{b1}}{\kappa^2} + \frac{1 + C_{b2}}{\sigma_{\tilde{v}}}\right)g\left[\frac{1 + C_{w3}^6}{g^6 + C_{w3}^6}\right]^{1/6}\rho\left(\frac{\tilde{v}}{y}\right)^2 \tag{3.30}$$

where,

$$g = r(1 + C_{w2}(r^5 - 1)) \tag{3.31}$$

and

$$r = \min\left[\frac{\tilde{v}}{\left(\sqrt{\frac{\partial u_i}{\partial x_j} - \frac{\partial u_j}{\partial x_i}} + \frac{\tilde{v}}{\kappa^2 y^2}f_{v2}\right)\kappa^2 y^2}, 10\right] \tag{3.32}$$

$S_{\tilde{v}}$ is a user-defined source parameter,

$$S_{\tilde{v}} = C_{b1}\left(1 - C_{t3}\exp\left(-C_{t4}\left(\frac{\tilde{v}}{v}\right)^2\right)\right)\left(\sqrt{\frac{\partial u_i}{\partial x_j} - \frac{\partial u_j}{\partial x_i}} + \frac{\tilde{v}}{\kappa^2 y^2} f_{v2}\right)\rho\tilde{v} \tag{3.33}$$

where,

$$f_{v2} = 1 - \frac{\left(\frac{\tilde{v}}{v}\right)^4 + \left(\frac{\tilde{v}}{v}\right) C_{v1}^3}{\left(\frac{\tilde{v}}{v}\right)^4 + \left(\frac{\tilde{v}}{v}\right)^3 + C_{v1}^3} \tag{3.34}$$

$\sigma_{\tilde{v}}$, C_{b1}, C_{b2}, C_{t3}, C_{t4}, κ, C_{w2}, C_{w3} and C_{v1} are constant values and v is molecular kinematic viscosity. y is defined as the distance from the field point to the closest wall.

Model Constants are as follows.

$$\sigma_{\tilde{v}} = \frac{2}{3}, \quad C_{b1} = 0.1355, \quad C_{b2} = 0.622, \quad C_{t3} = 1.2, \quad C_{t4} = 0.5,$$
$$\kappa = 0.41, \quad C_{w2} = 0.3, \quad C_{w3} = 2, \quad C_{v1} = 7.1,$$

3.3.2 k-ε Turbulence Model

The model is a two-equation model that has two transport equations for the simulation of the turbulent flow. The model is frequently used in CFD solutions and defined as the most effortless model because of the simple definitions requiring only initial or boundary conditions.

The model is especially designed for the specification of planar shear layers and the recirculating flows. For that reason, the most common and useful area of the model

is the cases with planar shear layers with small pressure gradients or with the Reynolds shear stresses are fundamental. The cases with complex shear layers or large pressure gradients could not be modeled easily and accurately with k-ε model due to the difference in the design aims.

The transformation of the k-ε model contains the rate of deformation as E_{ij}.

$$\frac{\partial}{\partial t}(\rho k) + \frac{\partial}{\partial x_i}(\rho k u_i) = \frac{\partial}{\partial x_j}\left[\frac{\mu_t}{\sigma_k}\frac{\partial k}{\partial x_j}\right] + 2\mu_t E_{ij} E_{ij} - \rho\varepsilon \qquad (3.35)$$

and,

$$\begin{aligned}\frac{\partial}{\partial t}(\rho\varepsilon) + \frac{\partial}{\partial x_i}(\rho\varepsilon u_i) &= \frac{\partial}{\partial x_j}\left[\frac{\mu_t}{\sigma_\varepsilon}\frac{\partial \varepsilon}{\partial x_j}\right] \\ &+ C_{1\varepsilon}\frac{\varepsilon}{k}2\mu_t E_{ij}E_{ij} - C_{2\varepsilon}\rho\frac{\varepsilon^2}{k}\end{aligned} \qquad (3.36)$$

where the turbulent viscosity μ_t is calculated as,

$$\mu_t = \rho C_\mu \frac{k^2}{\varepsilon} \qquad (3.37)$$

Model Constants are as follows.

$$\sigma_k = 1.00, \qquad \sigma_\varepsilon = 1.30, \qquad C_\mu = 0.09, \qquad C_{1\varepsilon} = 1.44, \qquad C_{2\varepsilon} = 1.92$$

3.3.3 k-ω SST Turbulence Model

The model combines the robust and compatible formulation of k-ω model near the wall and independence of k-ε model from far field next to the wall. The k-ω SST model is considerable similar to k-ω model with some exceptions. The standard k-ω model and the transformed k-ε model are multiplied by the blender function and summed with each other. The blender function has a value of 1 at the wall edge and activates the k-ω pattern. The function has a zero value further away from the wall

and causes activation of the k-ε model. Another difference between standard k-ω and SST is that in the equation, SST model includes the effect of the damped cross diffusion. For the SST model, the turbulent viscosity is redefined by taking into account the turbulent shear stress transport. As SST model has some additional features compared to standard k-ω model, the modelling constants are different from each other and the SST model can be considered as more reliable and compatible with several flow cases than k-ω model, especially at adverse pressure gradient flows.

k-ω SST model is quite similar to the standard k-ω model.

$$\frac{\partial}{\partial t}(\rho k) + \frac{\partial}{\partial x_i}(\rho k u_i) = \frac{\partial}{\partial x_i}\left(\Gamma_k \frac{\partial k}{\partial x_j}\right) + G_k - Y_k + S_k \qquad (3.38)$$

and

$$\frac{\partial}{\partial t}(\rho \omega) + \frac{\partial}{\partial x_i}(\rho \omega u_i) = \frac{\partial}{\partial x_i}\left(\Gamma_\omega \frac{\partial k}{\partial x_j}\right) + G_\omega - Y_\omega + D_\omega + S_\omega \qquad (3.39)$$

The term G_k represents the product of turbulent kinetic energies and is the same as in the standard k-ω model. G_ω represents the occurrence of ω and is calculated as defined in the standard k-ω model. Y_k and Y_ω represent the diffusion of k and ω from turbulence. D_ω is the cross-diffusion term. Γ_k and Γ_ω represent the effective spreading power of k and ω. S_k and S_ω are user defined source terms.

3.3.3.1 Effective Diffusion Modeling

The effective diffusion for k-ω SST is defined as dependent on σ_k and σ_ω as turbulent Prandtl numbers for k and ω.

$$\Gamma_k = \mu + \frac{\mu_t}{\sigma_k} \tag{3.40}$$

$$\Gamma_\omega = \mu + \frac{\mu_t}{\sigma_\omega} \tag{3.41}$$

Turbulent viscosity μ_t is calculated in Eq. (3.42).

$$\mu_t = \frac{\rho k}{\omega} \frac{1}{\max\left[\frac{1}{a^*}, \frac{SF_2}{a_1 \omega}\right]} \tag{3.42}$$

S is stated as the strain rate magnitude.

$$\sigma_k = \frac{1}{\frac{F_1}{\sigma_{k,1}} + \frac{1 - F_1}{\sigma_{k,2}}} \tag{3.43}$$

$$\sigma_\omega = \frac{1}{\frac{F_1}{\sigma_{\omega,1}} + \frac{1 - F_1}{\sigma_{\omega,2}}} \tag{3.44}$$

a^* dampens turbulent viscosity caused by low Reynolds number correction.

$$F_1 = \tanh(\phi_1^2) \tag{3.45}$$

$$\phi_1 = \min\left[max\left(\frac{\sqrt{k}}{0.09\omega y}, \frac{500\mu}{\rho y^2 \omega}\right), \frac{4\rho k}{\sigma_{\omega,2} D_\omega^+ y^2}\right] \tag{3.46}$$

$$D_\omega^+ = \max\left[2\rho \frac{1}{\sigma_{\omega,2}} \frac{1}{\omega} \frac{\partial k}{\partial x_j} \frac{\partial \omega}{\partial x_j}, 10^{-10}\right] \tag{3.47}$$

$$F_2 = \tanh(\phi_2^2) \tag{3.48}$$

$$\phi_2 = \max\left[2\frac{\sqrt{k}}{0.09\omega y}, \frac{500\mu}{\rho y^2 \omega}\right] \tag{3.49}$$

y is defined as the distance from the field point to the closest wall, while D_ω^+ denotes the positive term of the cross diffusion equation.

Model Constants are as follows.

$$\sigma_{k,1} = 1.176, \qquad \sigma_{\omega,1} = 2.0, \qquad \sigma_{k,2} = 1.0, \qquad \sigma_{\omega,2} = 1.168, \qquad a_1 = 0.31$$

3.3.3.2 Cross-Diffusion Modification

Since k-ω SST model consists of both k-ω and k-ε models, standard k-ε model is divided into two equations for the blending of two models and obtain k-ω SST model. The division is dependent on k and ω and the blending of two equations results in cross diffusion term, which is basically defined by k and ω terms.

$$D_\omega = 2(1 - F_1)\rho \frac{1}{\sigma_{\omega,2}} \frac{1}{\omega} \frac{\partial k}{\partial x_j} \frac{\partial \omega}{\partial x_j} \tag{3.50}$$

3.4 ANSYS Fluent

ANSYS Fluent offers its users a comprehensive modeling capability for various types of flows as compressible, incompressible, turbulent and laminar. The tool is capable of solving steady and transient flows. It has a large mathematical modeling library for modeling complex geometries and flow physics like heat transfer or chemical reaction problems.

ANSYS Fluent uses continuity and momentum equations for all flow problems. The energy equation is included to the calculations when the flow is compressible or the heat transfer is involved. If the flow is turbulent, addition of the transport equation is fundamental for the solution.

The typical vector notation is used for the definition of the continuity equation in ANSYS Fluent environment and the equation is applicable for both compressible and incompressible flows.

$$\frac{\partial \rho}{\partial t} + \nabla.\left(\rho \vec{V}\right) = S_m \tag{3.51}$$

The source S_m is the mass added to the continuous side from the discrete side or user-defined source.

Conservation of momentum equation can be stated as vector notation.

$$\frac{\partial \rho}{\partial t}.\left(\rho \vec{V}\right) + \nabla.\left(\rho \vec{V}\vec{V}\right) = -\nabla \mathrm{p} + \nabla.(\bar{\bar{\tau}}) + \rho \vec{g} + \vec{F} \tag{3.52}$$

CHAPTER 4

STEADY ANALYSES

The steady analyses are conducted for several flight conditions. The purpose is to investigate the optimum mesh and boundary conditions for converged and validated steady flow results, together with the examination of the flow field in the stable region, which is just before the buffet onset. For this purpose, the two dimensional NACA0012 airfoil model is constructed in Ansys Fluent Design Modeler environment. The mesh is constructed using the unstructured quadrilateral grid method. After the mesh is obtained, the boundary conditions for the required flight characteristics are applied to the flow for the analysis. All the analyses are conducted with density-based solver for viscous fluids. Several mesh resolutions and turbulence models have been applied in order to investigate the converged solution, which has the closest results to the wind tunnel data.

The three flow conditions corresponding to the conditions of the wind tunnel data [2] have been analyzed in the Ansys Fluent environment, marked with red in Figure 4.1 and listed in Table 4.1. Detailed explanation of all analyses and the detailed results made throughout the study was made on Dataset 4. For the other two conditions of Dataset 5 and 6, only the apparent results were shared. The grid spacing and Reynolds numbers for the condition are calculated as an input to the mesh and boundary conditions.

Table 4.1. *Analyzed Flow Condition* [2]

Dataset	***M***	***α (°)***
Dataset 4	0.800	1
Dataset 5	0.775	2
Dataset 6	0.725	4

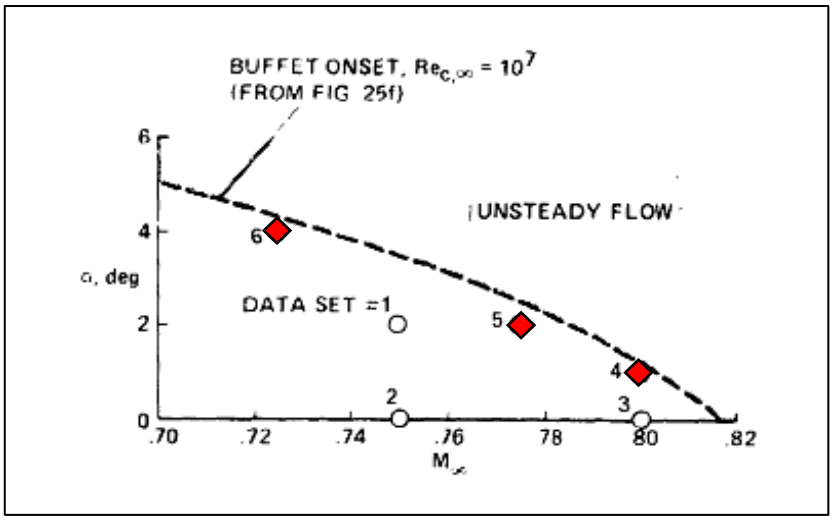

Figure 4.1. Buffet Onset Boundary of NACA0012 Airfoil [2]

4.1 Reynolds Number and Grid Spacing

The Reynolds number and the grid spacing effect the mesh quality as they indicate the difference between viscous forces and inertial forces around surface. The Reynolds number affects the boundary conditions directly in the analyses. In addition, the turbulence in the viscous flow is determined with Reynolds number. According to the Reynolds number of the determined flow condition, grid spacing is

obtained and applied to the mesh resolution in order to successfully resolve the boundary layer.

The required data in order to calculate the Reynolds number and grid spacing is stated in Table 4.2.

Table 4.2. *Standard Atmospheric Conditions of the Streamflow over Airfoil*

Dataset	***4 (M0.800 α=1°)***	***5 (M0.775 α=2°)***	***6 (M0.725 α=4°)***
a (m/s)	340.3	340.3	340.3
M	0.800	0.775	0.725
V (m/s)	272.24	263.73	246.72
ρ (kg/m^3)	1.225	1.225	1.225
l_{ref} (m)	0.2032	0.2032	0.2032

Firstly, Reynolds number is calculated with given conditions from Eq. (3.11).

The first layer of boundary layer thickness Δs is calculated according to the turbulent boundary layer theory. The y+ value is defined individually according to the turbulence model used for the solution.

The skin friction coefficient distribution is then calculated from Eq. (4.53).

$$C_f = \frac{0.026}{Re^{\frac{1}{7}}} \tag{4.53}$$

The momentum integral relation is calculated according to the skin friction coefficient.

$$\tau_{\text{wall}} = \frac{C_f \rho U_\infty^2}{2} \tag{4.54}$$

The friction velocity is obtained from the law of the wall in Eq. (4.55).

$$U_{fric} = \sqrt{\frac{\tau_{\text{wall}}}{\rho}} \tag{4.55}$$

Finally, the first layer of boundary layer thickness is obtained in relation with y+ and friction velocity.

$$\Delta s = \frac{y^+ \mu}{U_{\text{fric}} \rho} \tag{4.56}$$

The total thickness of boundary layer is calculated from turbulent boundary layer theory, in relation with Reynolds number and reference length.

$$\delta = \frac{0.37L}{Re^{0.2}} \tag{4.57}$$

The layer number is defined so as to obtain the required total thickness of the boundary layer from the first layer thickness. In order to obtain a smooth transition, a constant growth rate is used for the transition layers. In all of the mesh models of this study, growth rate is chosen as 1.2 for the transition layers.

Grid spacing values vary due to each analyzed flow condition. Thus, for each flow condition, the grid spacing value differs in the mesh resolution.

4.2 Mesh Independence

The solid model of the NACA0012 airfoil is constructed in Design Modeler tool of Ansys Fluent. The nodes on the airfoil are obtained as 201 points from Javafoil tool. O Type grid around airfoil and C Type grid through the control volume is applied. The airfoil chord is chosen as 0.2032 meters (8 inch) in order to be consistent with the wind tunnel model which is used for the wind tunnel tests of buffet onset

investigation in NASA Ames High Reynolds Number Facility [2]. The radius of the arc around airfoil leading edge is 7 times of the chord and the length of wall around airfoil is 14 times the chord. The grid is finer in a circle with radius of 1.5 times of the chord around the airfoil. The grid is also finer at the trailing edge of the airfoil through the outlet wall with a thickness around 1.4 times of the chord in order to examine the turbulent flow characteristics in detail due to flow separation on airfoil. The area out of the circle around airfoil and the rectangular field to the outer wall is coarser than the inside. The mesh pattern is retained with the growth rate as 1.2 between coarse and fine areas in order to keep the smooth transition with acceptable orthogonal quality and skewness ratios.

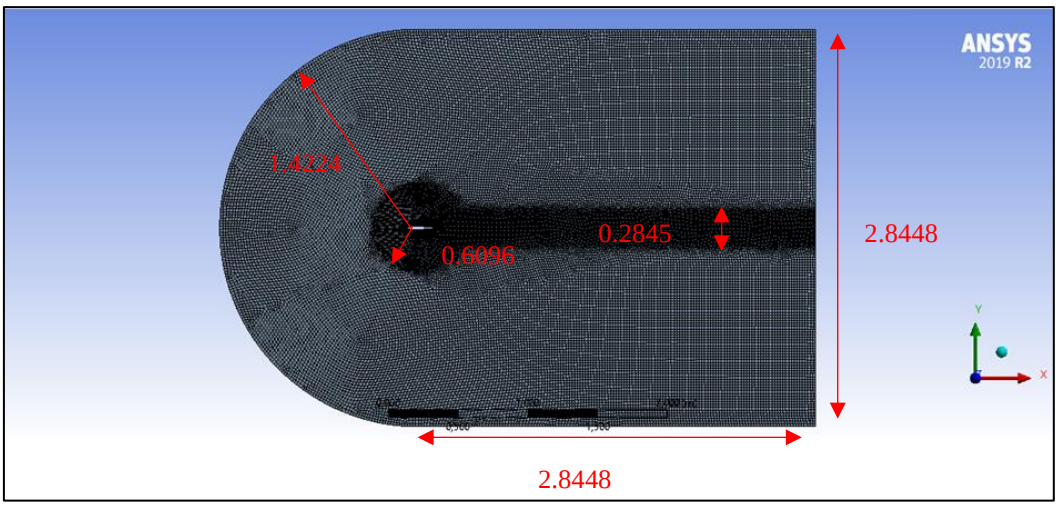

Figure 4.2. Sample Grid Spacing of Geometry with 89K Mesh Elements

Since the shape of trailing edge of the airfoil deviates from the origin for practical reasons during manufacturing, the CFD model is also trimmed at the trailing edge in order to be consistent with the wind tunnel model. The deviation from the mathematical model of NACA0012 airfoil was around $\Delta x/c \approx 0.01$. Due to the deviation in the trailing edge, the mesh resolution also includes the element sizing of the trailing edge surface individually. The mesh nodes of the trailing edge are chosen

in proportion to the mesh nodes of upper and lower airfoil surfaces so as not to affect the overall mesh resolution.

There are four different mesh resolutions for each flow condition. The first analysis is conducted for Dataset 4, M0.808 α=0.97° Re=4.1E+06. The Reynolds number and grid spacing is firstly calculated for these conditions as described in Section 4.1. The calculated grid spacing results and the mesh sizing features are stated for all four mesh resolutions in Table 4.4.

The first mesh resolution eventually consists of 88719 elements and this configuration is analyzed to obtain the pressure distribution around airfoil during transonic flow around buffet onset. Orthogonal quality is 0.95, skewness is 0.16 and the aspect ratio of the mesh is 44.28. The conditions are obtained from the dataset of wind tunnel results [2], which are stated as Dataset 4 in Table 4.2 previously.

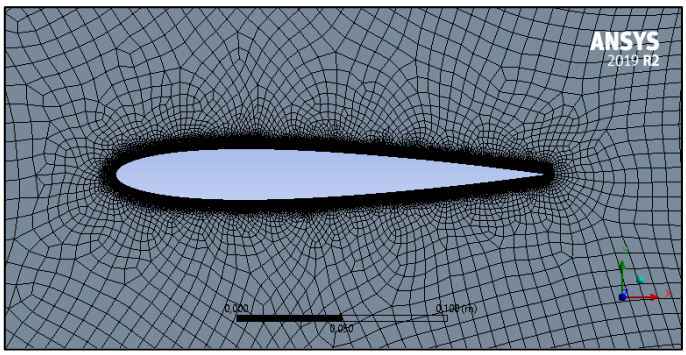

Figure 4.3. Grid Spacing of Geometry around Airfoil with 89K Mesh Elements

In order to define the optimum mesh resolution that gives the exact solution with minimum mesh elements, several mesh resolutions need to be analyzed for the same flow condition. The severity in the mesh resolution defines not only the minimum mesh element for the sufficient solution, but also the accuracy of the mesh resolution with several different mesh patterns. For this purpose, firstly two mesh patterns that have higher and a lower mesh element than the existing resolution have been

analyzed with the same flow condition. The ratio between new and existing mesh resolutions is kept as 1.5 as a rule of thumb.

The first grid resolution with higher mesh elements includes 137717 elements. There is a 4.6% decrease in skewness, 0.3% increase in orthogonal quality and 25.24% decrease in aspect ratio when the mesh elements are increased from 89K to 138K. The change in the mesh quality between these two mesh resolutions is in the acceptable region as the increase in elements with a ratio of 1.5 is taken into account while the inflation layer is kept as the same.

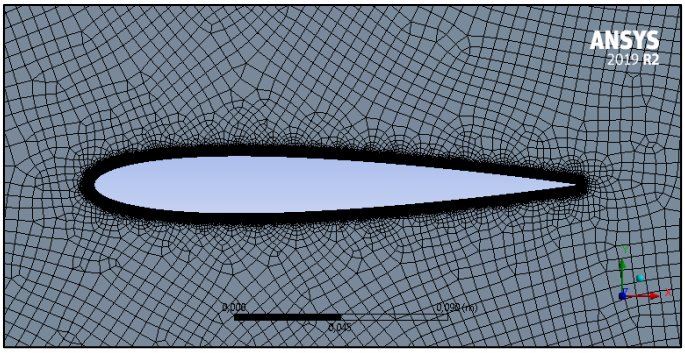

Figure 4.4. Grid Spacing of Geometry around Airfoil with 138K Mesh Elements

The grid resolution with second mesh pattern includes 208600 elements for keeping the same growth ratio as 1.5. There is a 10.3% decrease in skewness, 0.3% increase in orthogonal quality and 22.5% decrease in aspect ratio when the mesh elements are increased from 138K to 209K. The change in the mesh quality between these two mesh resolution is in the acceptable region as the increase in nodes with a ratio of 1.5 is taken into account while the inflation layer is kept as the same.

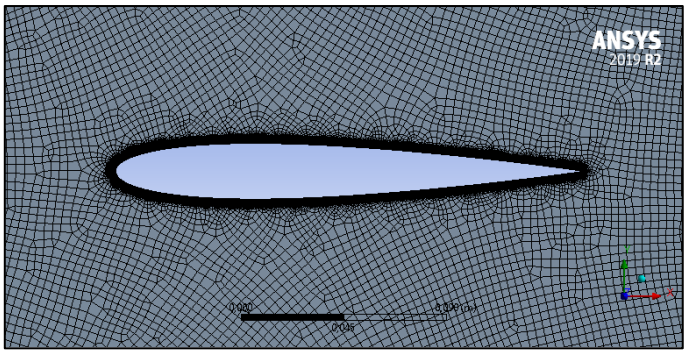

Figure 4.5. Grid Spacing of Geometry around Airfoil with 209K Mesh Elements

The grid resolution with lower mesh elements includes 61070 elements. There is a 11.4% increase in skewness, 0.5% decrease in orthogonal quality and 38.0% increase in aspect ratio when the mesh elements are decreased from 89K to 61K. The change in the mesh quality between these two mesh resolution is in the acceptable region as the decrease in nodes with a ratio of 1.5 is taken into account while the inflation layer is kept as the same.

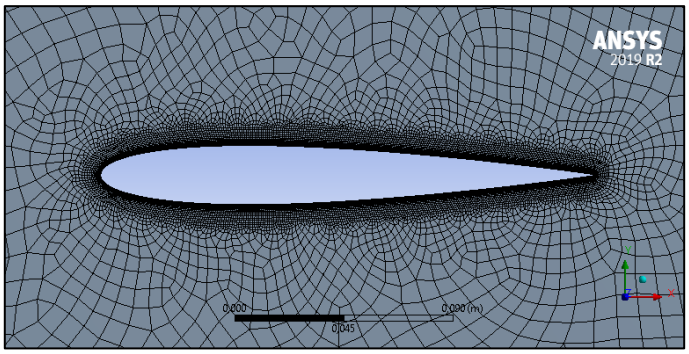

Figure 4.6. Grid Spacing of Geometry around Airfoil with 61K Mesh Elements

k-ω SST turbulence model is used during the whole analyses together with RANS equations to fundamentally reflect the turbulent flow behavior in the results with sufficient residuals. Density-based solver is considered without gravitational effect

in 2 dimensional flow. The residual tolerances are fixed to converge at least 10^{-4} up to 10000 iterations.

Table 4.3. *Analyzed Flow Conditions of Dataset 4*

Dataset 4	***(M0.808 α=0.97°)***
M	0.808
V (m/s)	274.96
ρ (kg/m3)	1.225
μ (kg/ms)	1.6693E-05
l_{ref} (m)	0.2032
Re	4.1E+06
α (°)	0.97

Table 4.4. *Sizing Features of Grid Spacing with Different Mesh Resolutions*

	Mesh Quantity	***61K***	***89K***	***138K***	***209K***
Body Sizing	Element Size (m)	0.0100	0.008	0.0052	0.0035
	Growth Rate	1.2	1.2	1.2	1.2
Edge Sizing	Airfoil Upper&Lower Surfaces (Number of Divisions)	500	1000	1500	2000
	Trailing Edge (Number of Divisions)	4	4	6	6
Inflation	Inflation Layer	43	43	43	43
	First Layer Thickness (m)	6.44866 E-07	6.44866 E-07	6.44866 E-07	6.44866 E-07
	Growth Rate	1.2	1.2	1.2	1.2
Mesh Quality	Nodes	61657	89517	138282	209085
	Elements	61070	88719	137717	208600
	Skewness	0.15339	0.16483	0.13121	0.11906
	Orthogonal Quality	0.94992	0.94824	0.96229	0.96726
	Aspect Ratio	64.253	44.283	28.755	19.261

When the pressure coefficient distributions of the all four different mesh grid resolutions are compared with each other and the wind tunnel data as stated in Figure 4.7, it is seen that the numerical solution of all four resolutions closely match with each other up to 40% of the chord. There is a slight difference in each solution in between 10% and 20% of chord at the upper surface of the airfoil. However, considering that the difference is small compared to the general distribution, it can be assumed as an acceptable variance among different grid patterns. After shock wave is observed, the results of 61K mismatches those of 89K, 138K and 209K at the lower surface between 40% and 60% of the chord, in contrast with the close match at the results of 89K, 138K and 209K in the same region. The pressure coefficient distribution on the lower surface with 89K, 138K and 209K is highly matching with wind tunnel data especially at the shock location, while the shock is captured slightly ahead of wind tunnel data at 61K mesh elements. Also, a mismatch occurs at upper surface between 50% and 60% of the chord. It is seen that the results are closely matched with wind tunnel data at the upper surface of the airfoil for 89K, 138K and 209K mesh elements; however, the resemblance is slightly lower for 61K mesh elements, especially at shock wave location. For that reason, it can be concluded that the mesh resolution with 61K elements is not adequate to simulate the specified flow characteristics around airfoil. Meanwhile, it is seen that the results are closely matched with wind tunnel data for 89K, 138K and 209K mesh elements and there are very slight differences between these three results. The resemblance of the results of 89K, 138K and 209K mesh states that the solution is independent from the mesh resolution. For this reason, 89K mesh is used for the oncoming studies since it is proven that the 89K mesh resolution gives convergent solution with minimum mesh elements.

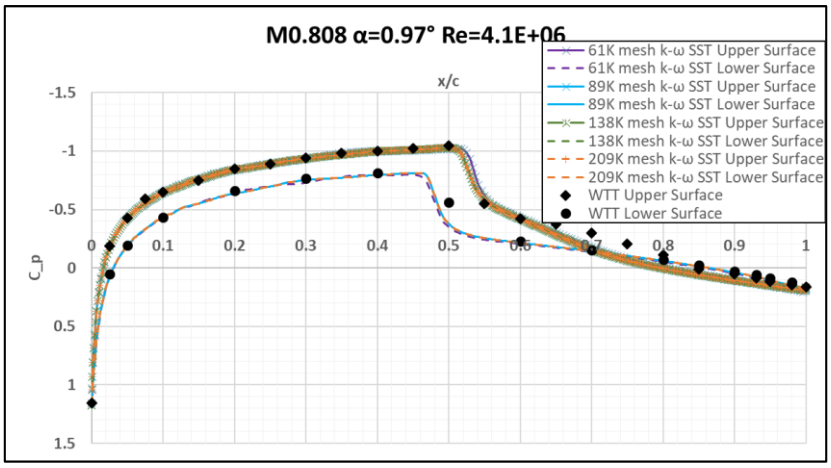

Figure 4.7. Comparison of Pressure Coefficient Distribution over Airfoil among 61K, 89K, 138K and 209K Mesh Resolution

4.3 Turbulence Model Set

In order to define the most compatible turbulence model that gives the exact solution with minimum deviation from the wind tunnel data, several turbulence models need to be used for the same flow condition. The severity in the turbulence model defines not only the best match with the wind tunnel data, but also the accuracy in the determination of the shock wave. The same face and edge sizing features with the same boundary layer thickness and y+ values are used for all turbulence models as specified in Section 4.2. 89K mesh resolution, which is the optimum mesh resolution that matches with the wind tunnel data with high accuracy is used at the turbulence model set analyses. Mainly three turbulence models are used for the analyses, which are Spalart-Allmaras, k-ε and k-ω SST. RANS equations used for the analysis and density-based solver is considered without gravitational effect in 2 dimensional flow. The residual tolerances are fixed to converge at least 10^{-4} up to 10000 iterations.

When the pressure coefficient distributions of the all three different turbulence models are compared with each other as depicted in Figure 4.8, it is seen that the numerical solution of three models closely match with each other up to 40% of the

chord. The results mismatches from each other at the lower surface between 40% and 60% of the chord and at the upper surface between 50% and 70% of the chord. At the lower surface, the shock capturing is quite close to each other for k-ε and Spalart-Allmaras models, while k-ω SST model predicts the pressure drop downstream of the shock approximately 2% of chord than the other two models. The prediction of the shock wave location is quite different for each turbulence model at the upper surface. The shock wave starts firstly at k-ω SST, then at k-ε and finally at Spalart-Allmaras turbulence model and the difference between the location of each pressure drop is approximately 2% of chord. k-ω SST turbulence model predicts the pressure drop at shock wave with the smallest chordwise distance between upper and lower surfaces of the airfoil (crisp shock capturing). When looking at the other turbulence models, it is seen that the distances between the locations of pressure drops of each airfoil surfaces have extended and the longest distance occurs at Spalart-Allmaras turbulence model (shock is smeared). The comparison between the numerical solution and wind tunnel data reveals that with k-ω SST, the shock is captured for both upper and lower surfaces with highest accuracy among all turbulence models. In this situation, it can be concluded that the most realistic prediction of the shock wave is obtained from the k-ω SST turbulence model due to slightly crisper resolution of the shock.

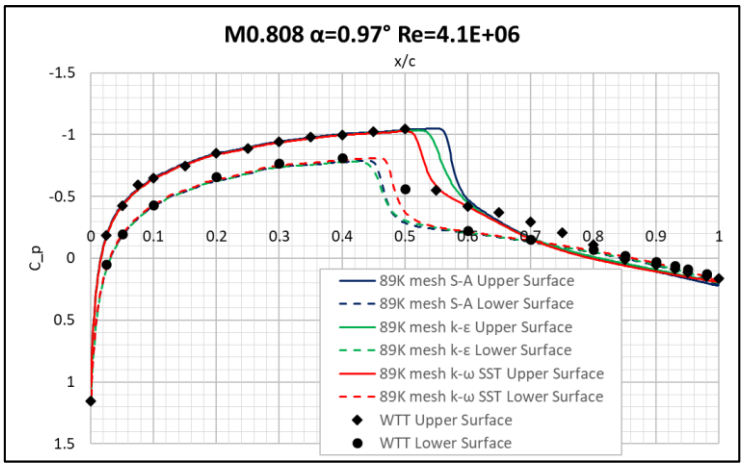

Figure 4.8. Comparison of Pressure Coefficient Distribution over Airfoil among Spalart-Allmaras, k-ε and k-ω SST Turbulence Models

4.4 Verification of the Numerical Analysis with Wind Tunnel Data

4.4.1 Verification of the Results for Low Reynolds Numbers

The numerical solution of the flow around airfoil which is enhanced through mesh independence and turbulence model set phases is compared with the existing wind tunnel data as stated in [2]. For each flow condition that has been listed at Section 4.1, the wind tunnel data that has been the closest to the flow condition is used for comparison. In this manner, the closest wind tunnel data to the flow condition that has been analyzed and stated as Dataset 4 in Table 4.5 exists as M0.808 α=0.97° Re=4.1E+06.

Table 4.5. *Analyzed Flow Conditions at Low Reynolds Number*

DataSet	***4 (M0.808 α=0.97°)***	***5 (M0.777 α=2.03°)***	***6 (M0.729 α=3.93°)***
M	0.808	0.777	0.729
V (m/s)	274.96	264.41	248.08
ρ (kg/m3)	1.225	1.225	1.225
μ (kg/ms)	1.6693E-05	1.6693E-05	1.5815E-05
l_{ref} (m)	0.2032	0.2032	0.2032
Re	4.1E+06	3.9E+06	3.9E+06
α (°)	0.97	2.03	3.93

The pressure coefficient distribution of the numerical solution of the flow condition that is specified in Table 4.5 is verified with the existing wind tunnel data as shown in Figure 4.9. The results closely match with wind tunnel data up to 50% of chord on the lower surface of airfoil. The shock location is predicted slightly downstream of the location of the wind tunnel results. However, the difference between numerical solution and the wind tunnel data is close to each other. After 60% of the chord, the results are again closely matched with wind tunnel data. The case in the upper surface is different than the lower surface. Up to 60% of the chord, the results are closely matched with wind tunnel data; however, in between 60% and 80% of the chord, the results diverge from the wind tunnel data.

The area between 40% and 60% of chord states the pressure distribution over upper and lower surfaces of the airfoil at shock wave. The flow around this area presents high local pressure and velocity changes due to shock wave. It is seen that the shock wave location and the pressure drop at the shock wave is predicted accurately at both

upper and lower surface of the airfoil with high accuracy compared to wind tunnel data.

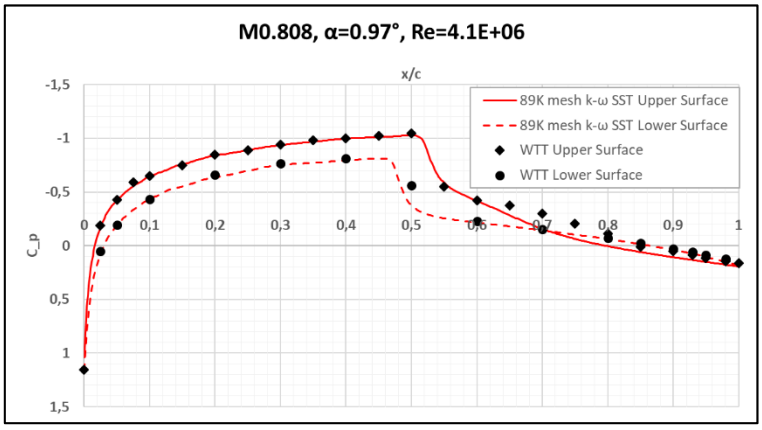

Figure 4.9. Verification of the Numerical Result of Dataset 4 with Wind Tunnel Data

The same methodology for Dataset 4 is applied to the Dataset 5 and Dataset 6 in terms of mesh independence and turbulence model set studies. After the mesh resolution and the turbulence model is determined, the results are verified with the applicable conditions of wind tunnel data as stated in [2].

For each flow condition that has been listed at Section 4.1, the wind tunnel data that has been the closest to the flow condition is used for comparison. In this manner, the closest wind tunnel data to the flow condition that has been analyzed and stated as Dataset 5 in Table 4.5 exists as M0.777 α=2.03° Re=3.9E+06.

The pressure coefficient distribution of the numerical solution of the flow condition that is specified in Table 4.5 is verified with the existing wind tunnel data as shown in Figure 4.10. The results closely match with wind tunnel data on the lower surface of airfoil. The case in the upper surface is different than the lower surface. Up to 45% of the chord, the results are not fully matched with wind tunnel data; however, the trend between the results and the wind tunnel data is very similar. The numerical

solution predicts the pressure distribution slightly lower than real value; however, the difference can be considered as small. Between 45% and 55% of the chord, the shock capturing of the numerical solution is highly accurate when it is compared to the wind tunnel data. After 55% of the chord, the pressure distribution is predicted lower than the wind tunnel data. When looking the overall pressure distribution results, it is seen that the numerical results predict consistently lower pressure coefficients relative to the wind tunnel data. It is seen that the numerical results predict the pressure drop at the shock wave at the upper surface of the airfoil with high accuracy based on wind tunnel data.

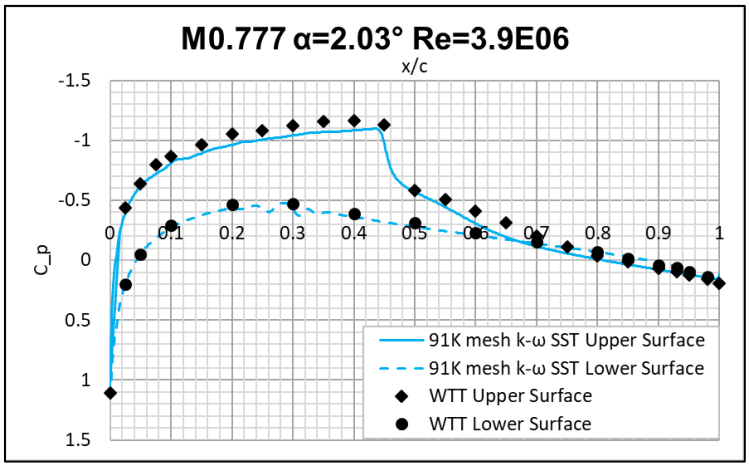

Figure 4.10. Verification of the Numerical Result of Dataset 5 with Wind Tunnel Data

For each flow condition that has been listed at Section 4.1, the wind tunnel data that has been the closest to the flow condition is used for comparison. In this manner, the closest wind tunnel data to the flow condition that has been analyzed and stated as Dataset 6 in Table 4.5 exists as M0.729 α=3.93° Re=3.9E+06.

The pressure coefficient distribution of the numerical solution of the flow condition that is specified in Table 4.5 is verified with the existing wind tunnel data as shown in Figure 4.11. The results closely match with wind tunnel data up to 90% of chord

on the lower surface of airfoil. At the upper surface of the airfoil, the results are matched with wind tunnel data up to 10% of the chord. Between 10% and 32% of the chord, the numerical solution predicts the pressure distribution slightly lower than real value. Although the pressure at beginning of the shock wave is slightly lower than wind tunnel data, the shock location and the pressure drop during shock is captured with high accuracy. In fact, after shock, the results are closely matched with wind tunnel data after 35% of the chord. It is seen that the numerical results predict the pressure drop at the shock wave at the upper surface of the airfoil with high accuracy based on wind tunnel data.

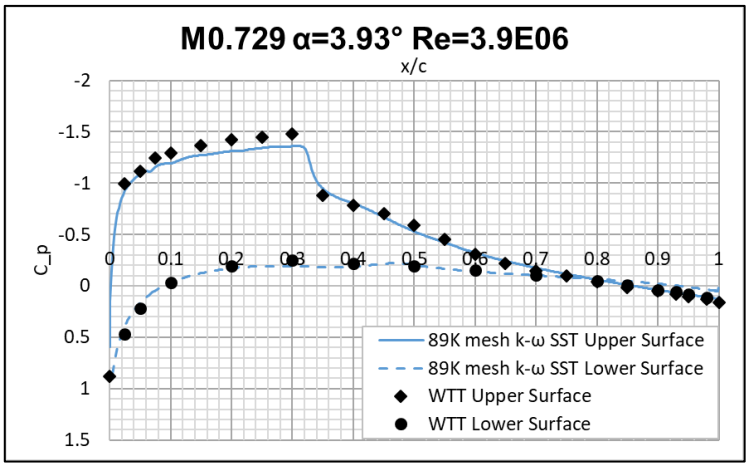

Figure 4.11. Verification of the Numerical Result of Dataset 6 with Wind Tunnel Data

4.4.2 Verification of the Results for High Reynolds Numbers

After the verification of the numerical solution with wind tunnel data for low Reynolds Number, the similar flow conditions are verified for high Reynolds Number in order to investigate the high Reynolds Number characteristics of the buffet. The further investigation of the buffet onset at high Reynolds numbers are stated with the verification of the transient analyses. The increase in the Reynolds

number directly affects the viscous and inertial forces on the flow through airfoil. Due to the variation of viscous and inertial forces on high Reynolds number, the shock wave location on the upper and the lower surfaces of the airfoil can vary. In order to capture these changes and reflect the flow behavior accurately, the mesh resolution is increased and the new boundary layer thickness is determined depending on the new Reynolds number and related flow conditions.

The mesh model that satisfies a convergent solution to the flow conditions with high Reynolds number is constructed with the same NACA0012 airfoil design points that are specified before in Section 4.2. C Type grid around airfoil and through the control volume is applied. The radius of the arc around airfoil leading edge is increased to 10 times of the chord and the length of wall around airfoil is increased to 20 times of the chord. The grid is finer in a circle with radius of 5 times of the chord around the airfoil. The grid is also finer at the trailing edge of the airfoil through the outlet wall with a thickness around 10 times of the chord in order to examine the turbulent flow characteristics in detail due to flow separation on airfoil as it is defined in detail in Figure 4.12. The fineness of the mesh resolution around and after trailing edge is increased in order to capture the instabilities in the boundary layer flow at the trailing edge better as it is stated in Figure 4.13. The area out of these circles around airfoil and the rectangular field to the outer wall is coarser than the inside. The mesh pattern is retained with the growth rate as 1.2 between coarse and fine areas in order to keep the smooth transition with acceptable orthogonal quality and skewness ratios.

The mesh resolution to satisfy this condition is obtained with 428K mesh elements. Orthogonal quality is 0.97, skewness is 0.10 and the aspect ratio of the mesh is 22.14. The detailed information about the mesh is stated in Table 4.6 and the mesh resolution around airfoil is stated in Figure 4.12 and Figure 4.13. Reynolds number and grid spacing is calculated for three conditions as described in Section 4.1, and a common mesh model is obtained with 428K mesh elements for a single boundary layer value that is accurate for all three conditions.

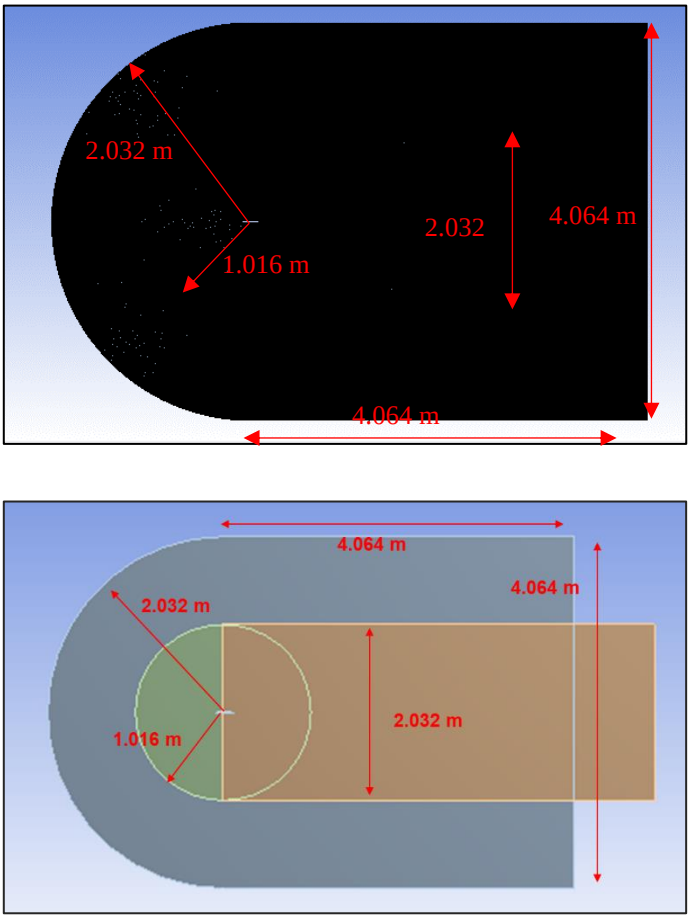

Figure 4.12. Sample Grid Spacing of Geometry with 428K Mesh Elements

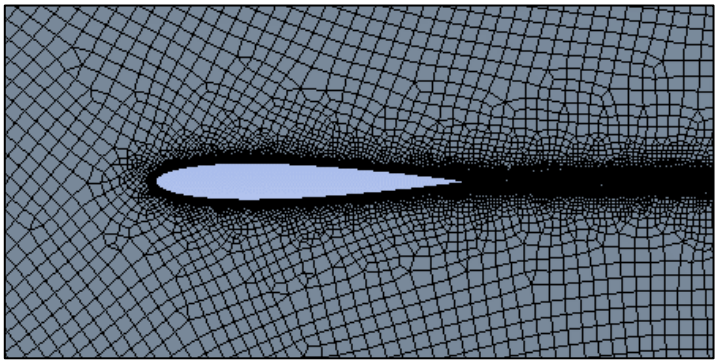

Figure 4.13. Grid Spacing of Geometry around Airfoil with 428K Mesh Elements

Table 4.6. *Sizing Features of Grid Spacing with 428K Mesh Elements*

	Mesh Quantity	***428K***
Body Sizing	Element Size (m)	0.01
	Growth Rate	1.2
Edge Sizing	Airfoil Upper&Lower Surfaces (Number of Divisions)	1000
	Trailing Edge (Number of Divisions)	6
Inflation	Inflation Layer	47
	First Layer Thickness (m)	2.74092E-07
	Growth Rate	1.2
Mesh Quality	Nodes	427992
	Elements	428124
	Skewness	0.09717
	Orthogonal Quality	0.97754
	Aspect Ratio	22.142

Table 4.7. *Analyzed Flow Conditions at High Reynolds Number*

DataSet	***4 (M0.793 α=1.00°)***	***5 (M0.775 α=2.05°)***	***6 (M0.726 α=3.91°)***
M	0.793	0.775	0.726
V (m/s)	269.86	263.73	247.06
ρ (kg/m3)	1.225	1.225	1.225
μ (kg/ms)	6.52E-06	6.6E-06	6.6E-06
l_{ref} (m)	0.2032	0.2032	0.2032
Re	10.3E+06	9.9E+06	9.3E+06
α (°)	1.00	2.05	3.91

For each flow condition that has been listed at Section 4.1, the wind tunnel data that has been the closest to the flow condition is used for comparison for the high Reynolds number case. In this manner, the closest wind tunnel data to the flow condition that has been analyzed and stated as Dataset 4 in Table 4.7 exists as M0.793 α=1.00° Re=10.3E06.

The pressure coefficient distribution of the numerical solution of the flow condition verified with the existing wind tunnel data as shown in Figure 4.14. The results closely match with wind tunnel data up to 60% of the chord on the upper surface of airfoil. However, the results are not closely matched with the wind tunnel data after 48% of the chord at the lower surface. It is seen that the pressure drop on the lower surface cannot be estimated correctly with the current mesh resolution and turbulence model. The shock location is predicted upstream than the wind tunnel data. After 60% of the chord, the results diverge from the wind tunnel data. It is seen that the numerical results predict consistently lower pressure coefficients especially

at the lower surface relative to the wind tunnel data. It is seen that the numerical results incorrectly predict the pressure drop at the shock wave at the lower surface for the high Reynolds number of the airfoil based on wind tunnel data.

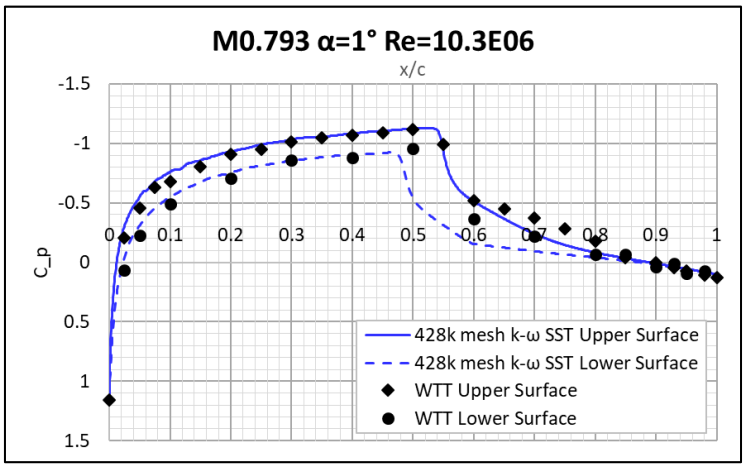

Figure 4.14. Verification of the Numerical Result of Dataset 4 with Wind Tunnel Data at High Reynolds Number

For the verification of the results of Dataset 5, the closest wind tunnel data to the flow condition that has been analyzed and stated as Dataset 5 in Table 4.7 exists as M0.775 α=2.05° Re=9.9E+06.

The pressure coefficient distribution of the numerical solution of the flow condition that is specified in Table 4.7 verified with the existing wind tunnel data as shown in Figure 4.15. The results closely match with wind tunnel data on the lower surface of airfoil. There is a slight difference between numerical results and wind tunnel data from 20% to 60% of the airfoil lower surface; however, this difference can be considered as small. The numerical solution predicts the pressure distribution in high accuracy at the upper surface, especially at the shock location. The location of the shock wave and the pressure drop during shock is closely matched with wind tunnel data up to 55% of the chord. After 55% of the chord, the numerical solution predicts the pressure distribution slightly lower than wind tunnel data. It can be concluded

that the turbulence in the boundary layer after shock wave is not predicted with high accuracy; however, the difference can be considered as small. When looking the overall pressure distribution results, it is seen that the numerical results predict pressure coefficients with high accuracy relative to the wind tunnel data.

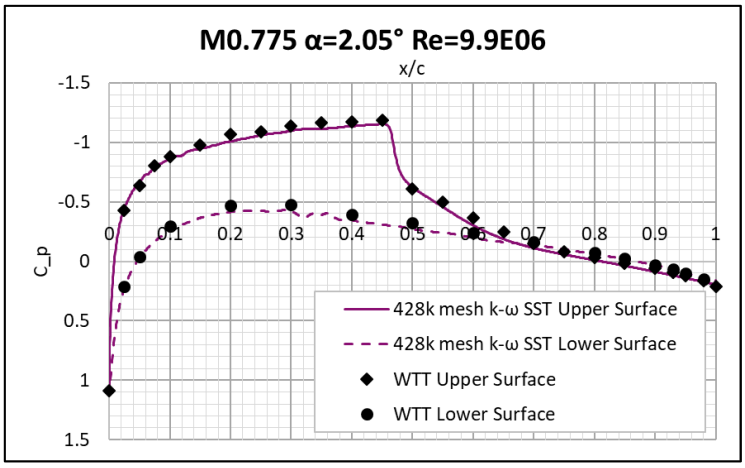

Figure 4.15. Verification of the Numerical Result of Dataset 5 with Wind Tunnel Data at High Reynolds Number

For the verification of the results of Dataset 6, the closest wind tunnel data to the flow condition that has been analyzed and stated as Dataset 6 in Table 4.7 exists as M0.726 α=3.91° Re=9.3E+06.

The pressure coefficient distribution of the numerical solution of the flow condition that is specified in Table 4.7 verified with the existing wind tunnel data as shown in Figure 4.16. The results closely match with wind tunnel data on the lower surface of airfoil. There is a slight difference between numerical results and wind tunnel data from 35% to 55% of the airfoil lower surface; however, the difference is considerably small. The numerical solution predicts the pressure distribution in high accuracy at the upper surface, especially at the shock location. The shock is captured at the upper surface with high accuracy and the flow behavior after shock is simulated well up to trailing edge. When looking the overall pressure distribution results, it is seen that

the numerical results predict pressure coefficients with high accuracy relative to the wind tunnel data.

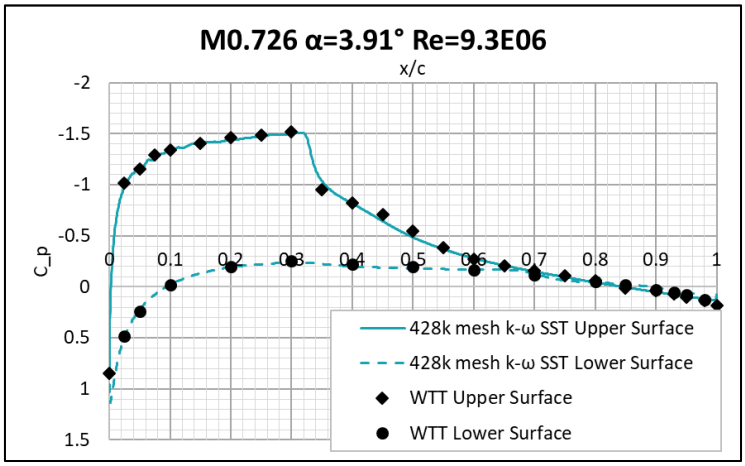

Figure 4.16. Verification of the Numerical Result of Dataset 6 with Wind Tunnel Data at High Reynolds Number

CHAPTER 5

TRANSIENT ANALYSES

The transient analyses are conducted for several flight conditions. The purpose is to investigate the time variant flow behavior around airfoil and determine the onset of the oscillating flow at transonic speeds with certain conditions. For this purpose, the two dimensional NACA0012 airfoil model is constructed in Ansys Fluent Design Modeler environment. The mesh of the two-dimensional model has been optimized as stated in Section 4.

After the mesh is obtained, the boundary conditions for the required flight characteristics are applied to the flow at the analysis. All the analyses are conducted with density-based solver for viscous fluids in two-dimensional flow. U-RANS equations with k-ω SST turbulence model is used for the transient analyses.

The analyses are divided into two parts as steady and unsteady flow. In order to determine and define the changes in the transonic flow field around buffet onset, the steady analyses are conducted in the stable flow region, which correspond to the area below buffet onset as colored green in Figure 5.1. The unsteady analyses are aimed to see the oscillating shock wave and determine the oscillation frequency around oscillating shock. With this aim, the unsteady analyses are conducted at the area above the buffet onset as colored orange in Figure 5.1. The angle of attack of the unsteady transient flow analysis is set by adding two degrees to the steady flow condition, the Mach number is kept the same as steady flow with a fixed value of Reynolds number in unsteady flow as 4E+06. In this way, the transition from steady to unsteady flow can be observed due to the angle of attack change during transonic flow as the analysis condition shifts upward and pass over buffet onset as seen in Figure 5.1.

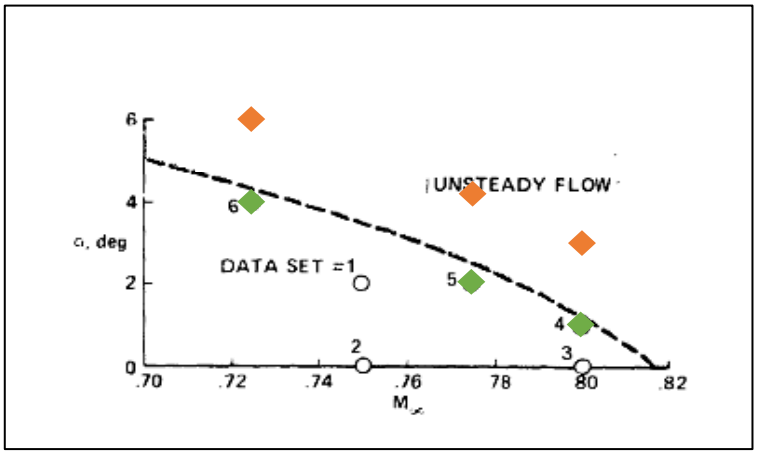

Figure 5.1. Transient Flow Analysis Conditions [2]

5.1 Steady Flow

So far three conditions have been analyzed in the Ansys Fluent as listed in Table 5.1.

Table 5.1. *Analyzed Flow Conditions for Steady Flow* [2]

Dataset	***M***	***α(°)***
Dataset 4	0.800	1
Dataset 5	0.775	2
Dataset 6	0.725	4

The first analysis is conducted for M0.800 α=1° Re=3.7E+06. The steady transient analysis is conducted from the mesh configuration that has 428K mesh elements. The mesh optimization and the validation of the numerical results are stated in

Section 4.4.2. The model is analyzed for 2 seconds with a 0.0001 second timestep. The residual tolerances are fixed to converge at least 10^{-6} up to 20 iterations per timestep.

The time variant lift, drag, moment coefficients and static pressure distribution for the airfoil are presented in Figure 5.2. Static pressure is the average of the measurements of the airfoil upper and lower surface pressure values. The oscillations occurring on all of the coefficients and static pressure in the first 0.25 seconds are caused by the disturbance of the streamflow when it suddenly reaches the airfoil. The oscillations are damped up to 0.5 seconds when the flow balances and the uniform flow is reached as streamflow. After 0.5 seconds, it is seen that there is no evidence of a shock oscillation on the flow as all of the coefficients and static pressure distribution over time on airfoil reach a constant value.

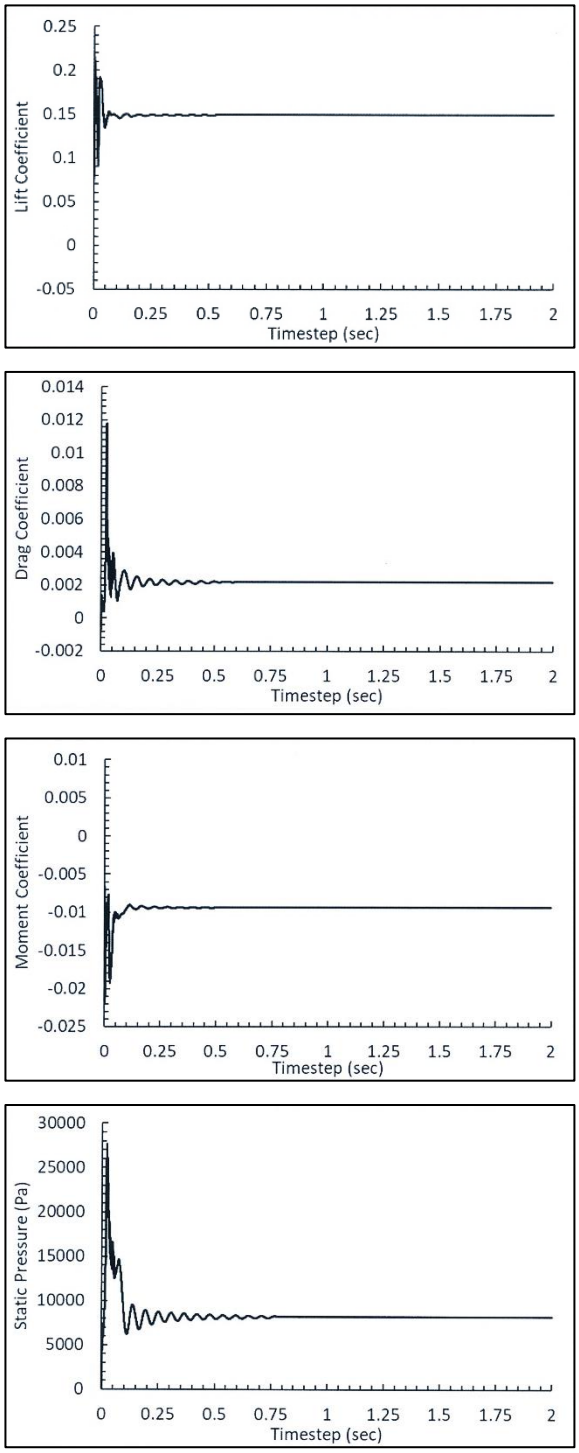

Figure 5.2. Lift, Drag, Moment Coefficient and Static Pressure Variation over Time at M0.800, α=1°, Re=3.7E+06

The second analysis is conducted for M0.775 α=2° Re=3.7E+06. The steady transient analysis is conducted from the mesh configuration that has 428K mesh elements. The mesh optimization and the validation of the numerical results are stated in Section 4.4.2. The model is analyzed for 2 seconds with a 0.0001 second timestep. The residual tolerances are fixed to converge at least 10^{-6} up to 20 iterations per timestep.

The time variant lift, drag, moment coefficients and static pressure distribution for the airfoil are presented in Figure 5.3. The oscillations seem to be damped after around 0.3 seconds when the uniform flow is obtained as streamflow. The buffet is not seen when looking at the converged steady distribution of the coefficients over time.

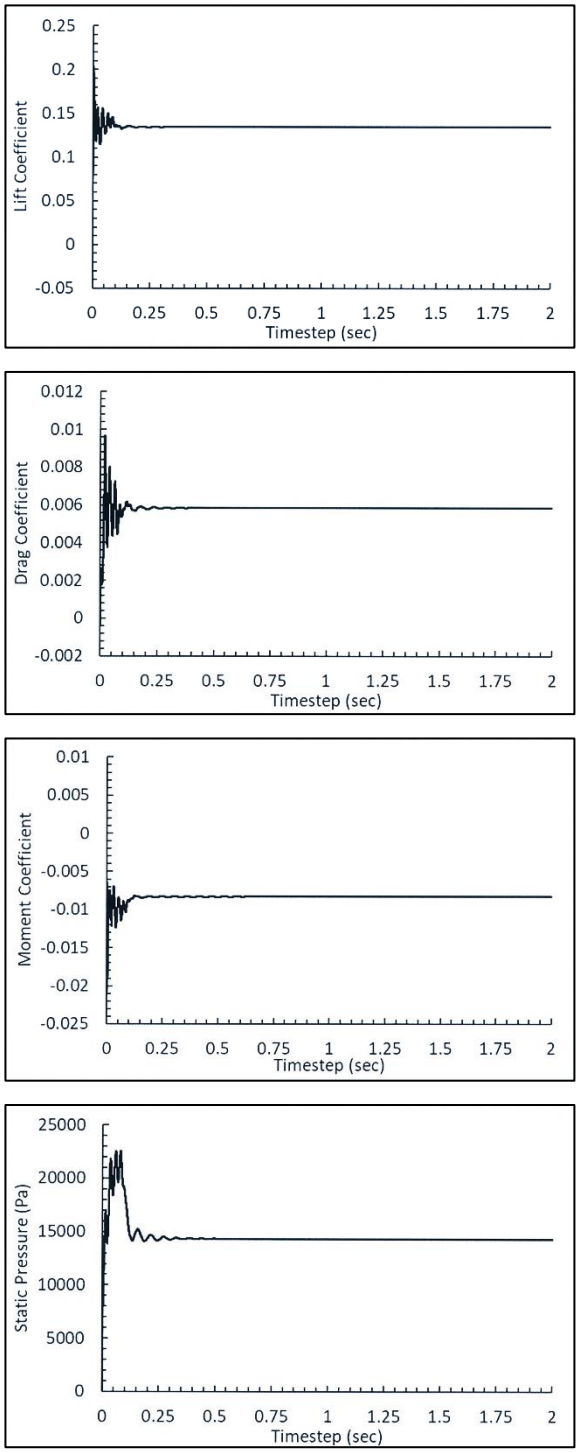

Figure 5.3. Lift, Drag, Moment Coefficient and Static Pressure Variation over Time at M0.775, α=2°, Re=3.7E+06

The third analysis is conducted for M0.725 α=4° Re=3.4E+06. The steady transient analysis is conducted from the mesh configuration that has 428K mesh elements. The mesh optimization and the validation of the numerical results are stated in Section 4.4.2. The model is analyzed for 2 seconds with a 0.0001 second timestep. The residual tolerances are fixed to converge at least 10^{-6} up to 20 iterations per timestep.

The time variant lift, drag, moment coefficients and static pressure distribution for the airfoil are presented in Figure 5.4. Like the steady analyses of Dataset 4 and Dataset 5, the streamflow is reached after around 0.25 seconds. As the stable variations of the coefficients indicated, the buffet is not seen at this flow conditions.

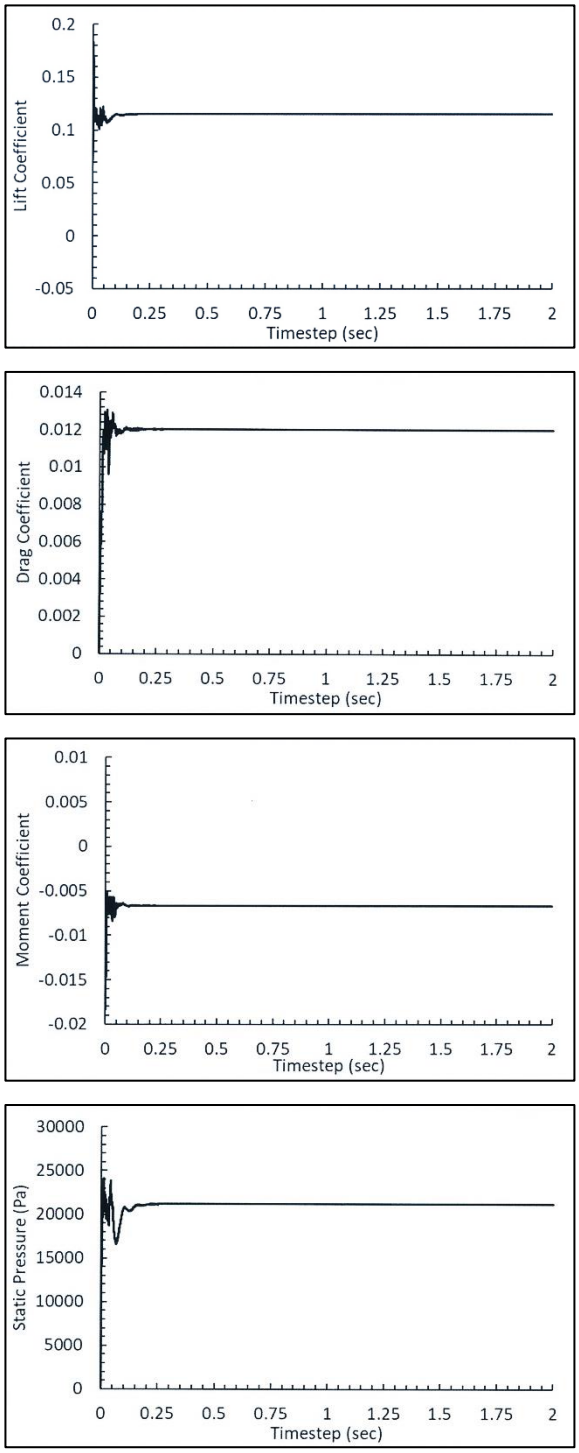

Figure 5.4. Lift, Drag, Moment Coefficient and Static Pressure Variation over Time at M0.725, α=4°, Re=3.4E+06

Considering all three flow conditions that are analyzed with numerical solutions, it is seen that the flow is settled and streamflow is obtained for all three conditions that are in the stable region of buffet onset curve. However, the convergence obtained in different durations for all three conditions. The convergence durations continuously decrease as the flow conditions change from Dataset 4 to Dataset 5 and then Dataset 6. It is seen that, as the Mach number decreases, and the critical angle of attack increases as a function of the critical Mach number, the convergence of the flow through a stable region occurs in a shorter duration.

5.2 Unsteady Flow

So far three conditions have been analyzed in the Ansys Fluent as listed in Table 5.2.

Table 5.2. *Analyzed Flow Conditions for Unsteady Flow* [2]

Dataset	***M***	***α (°)***	***Re***
Dataset 4	0.800	4	4E+06
Dataset 5	0.775	4	4E0+6
Dataset 6	0.725	6	4E+06

The first analysis is conducted for M0.800 α=4° Re=4E+06. The steady transient analysis is conducted from the mesh configuration that has 428K mesh elements. The mesh optimization and the validation of the numerical results are stated in Section 4.4.2. The model is analyzed for 2 seconds with a 0.0001 second timestep. The residual tolerances are fixed to converge at least 10^{-6} up to 20 iterations per timestep.

The time variant lift, drag and moment coefficients and static pressure distribution for the airfoil are illustrated in Figure 5.5, together with the power spectral density variations of the same coefficients over logarithmic scale of frequency. The constant oscillating behavior of the flow is seen from lift, drag and moment coefficients and additionally, static pressure fluctuations. The first peak on the frequency around 0.1 seconds is due to the disturbance of the streamflow when it suddenly reaches the wing. The undamped oscillating behavior which is common in lift, drag, moment coefficient and static pressure variations over time is the evidence of a shock oscillation.

When the power spectral density variations of lift, drag, moment coefficients and static pressure is investigated, the peak point is seen at 29.7 Hz. The peak point indicates the dominant frequency of the buffet. The other bumps on the curve is due to the noise on the data.

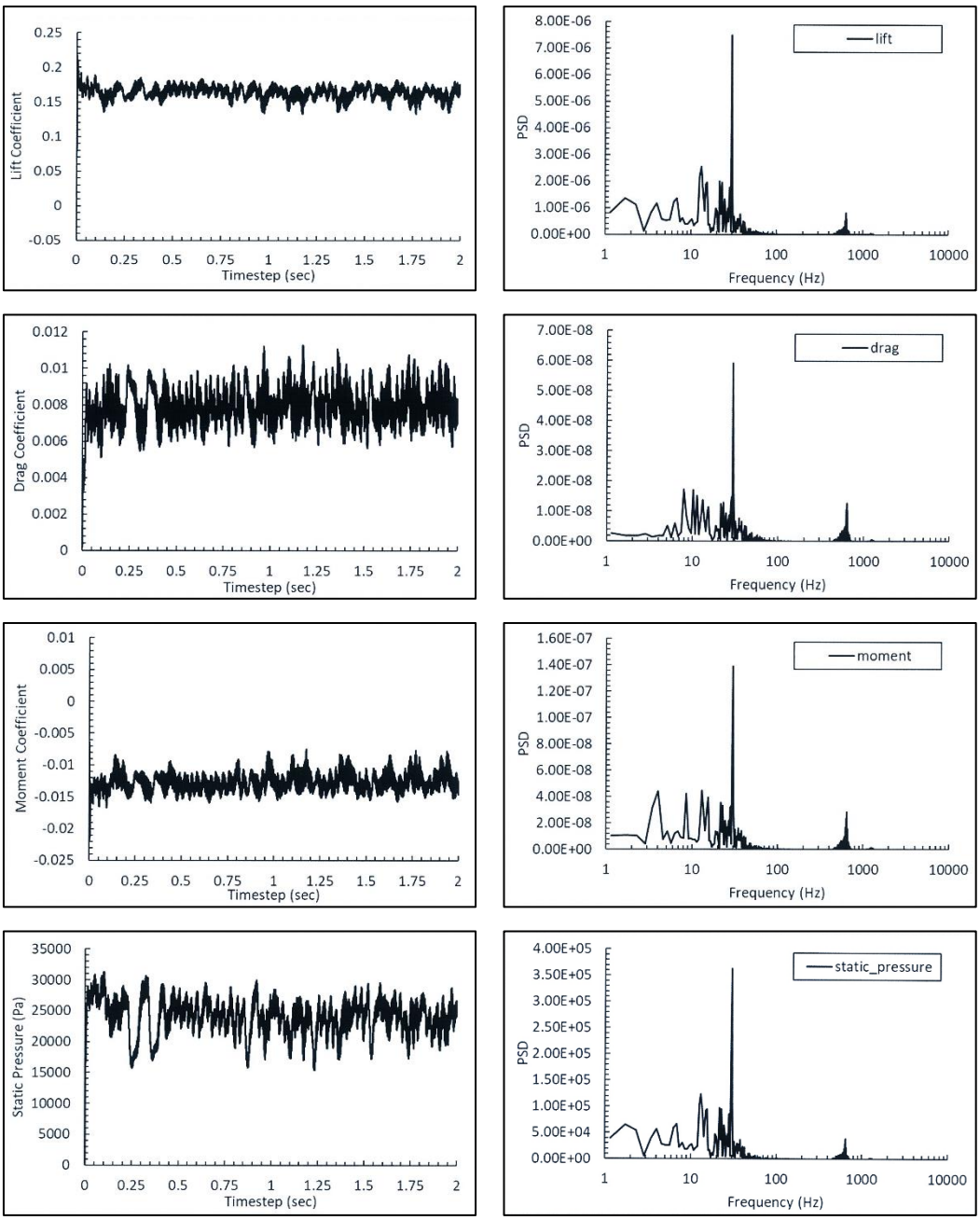

Figure 5.5. Lift, Drag, Moment Coefficient and Static Pressure Variation over Time and the Power Spectral Density Variations over Frequency at M0.800, α=4°, Re=4E+06

The dominant frequency is measured as 29.7 Hz in all power spectral density plots of lift, drag, moment and static pressure. Since the measured frequency is the same for all parameters, it is determined as the buffet frequency. The numerical results cannot be compared with wind tunnel data for the current flow condition with low Reynolds number due to lack of wind tunnel data.

The pressure and velocity u waveforms of the upper and lower surfaces of the airfoil at 50% and 80% of the chord is depicted in Figure 5.6. The waveforms are calculated especially at 50% and 80% of the chord, since the shock is generated at 50% of the chord and its interaction with the boundary layer becomes significant towards trailing edge. The frequency of the oscillations is higher at the upper surface then lower surface for the pressure waveforms. The frequency of velocity u waveform at 50% of the chord is quite low on upper surface. In addition, the difference in the frequencies between 50% and 80% of the chord indicates that at the upper surface, the oscillation frequency increases when the flow approaches to the trailing edge. It is observed that the oscillation behaviors of the pressures and u velocities vary for each individual location on airfoil at both surfaces. The dominant frequencies of each four locations are different than each other. For that reason, it is highly difficult to obtain a dominant buffet frequency from a local point on airfoil. Instead, the approach for the determination of the buffet frequency is to obtain the dominant frequency from the variations of the static pressure or lift, drag, moment coefficients with time.

The average location of the shock oscillations can be predicted from the variations in the frequencies of the wavelengths. In this manner, the oscillations are not started at 50% of the airfoil on upper surface due to the low frequencies of wavelengths at this point. The frequencies are increased highly at 80% of the chord, which is the indication of the higher oscillations at boundary layer. The shock oscillations started at a point in between 50% and 80% of the chord on upper surface. The oscillation frequencies at the lower surface are not quite different from each other, which indicates that oscillating shock does not exist at the lower surface.

Upper Surface:

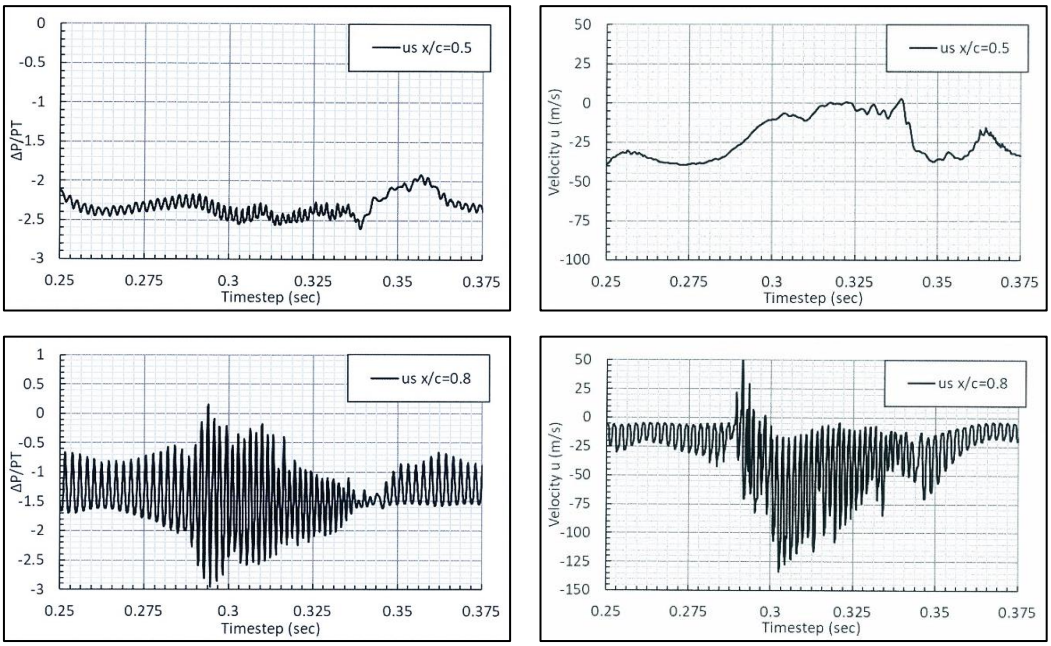

Lower Surface:

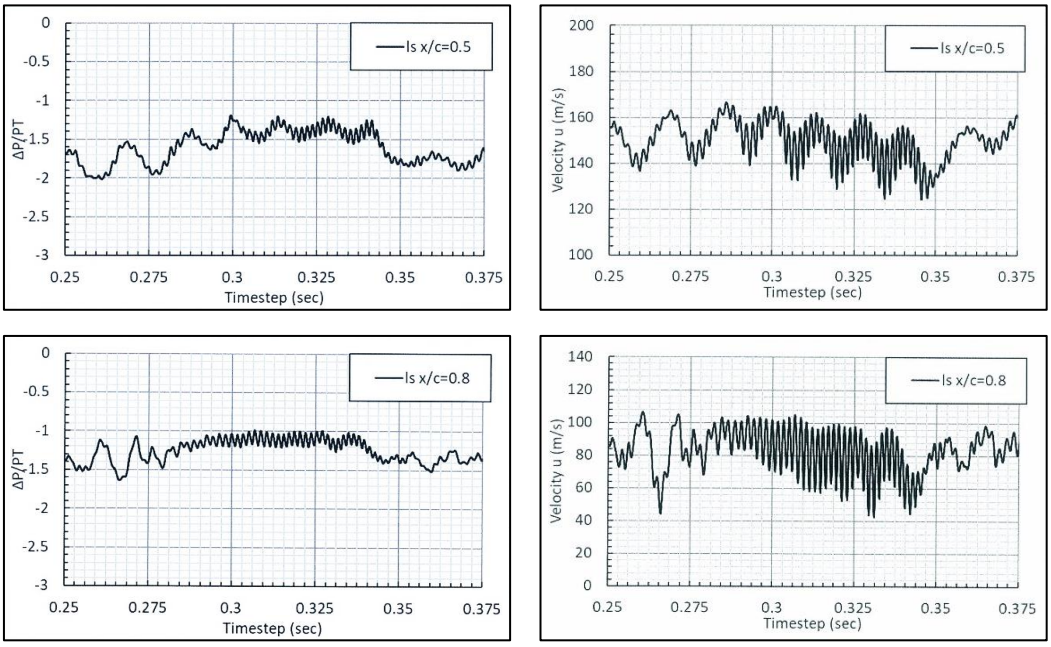

Figure 5.6. Comparison of Upper and Lower Surface Pressure and Velocity u Waveforms over Time at M0.800, α=4°, Re=4E+06

The pressure waveforms at 50% and 80% of the chord is depicted in Figure 5.7. The difference of the results between Figure 5.6 and Figure 5.7 is that the mean value is obtained by the subtraction of the pressure waveforms at the upper surface from the lower surface for 50% and 80% of the chord. The results give better information about the mean pressure variations at 50% and 80% of the chord. Hence, the change in oscillation frequency can be observed better as the flow moves towards the trailing edge. The oscillation frequency on the flow increases when moving from 50% of the chord to the 80% of the chord. Since the separation on the boundary layer due to the interaction with shock wave oscillation increases when the flow approaches to the trailing edge, the increase in the frequency is an expected result.

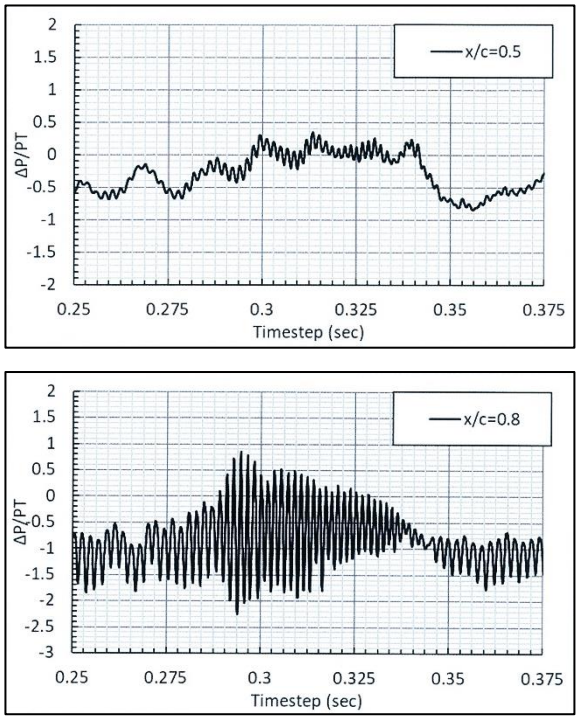

Figure 5.7. Pressure Waveforms over Time at M0.800, α=4°, Re=4E+06

The frequency of the oscillating behavior of buffet is measured as 29.7 Hertz for the unsteady transient flow. The oscillation about 29.7 Hertz in this flow condition creates a Strouhal number as 0.14. A complete comparison cannot be made since

there is no data with a low Reynolds number as in this flow condition in wind tunnel results [2]. However, for the general comparison, the Strouhal number of the unsteady motion is relatively low for all of the values of the wind tunnel data. The possible reason is that the analyzed flow condition is at low Reynolds number; whereas the Strouhal numbers stated in wind tunnel results are for high Reynolds number. In this manner, for the current flow conditions, the oscillating shock behavior exists; however, it is not obvious that the flow reaches the buffet onset.

The second analysis is conducted for M0.775 α=4° Re=4E+06. The steady transient analysis is conducted from the mesh configuration that has 428K mesh elements. The mesh optimization and the validation of the numerical results are stated in Section 4.4.2. The model is analyzed for 2 seconds with a 0.0001 second timestep. The residual tolerances are fixed to converge at least 10^{-6} up to 20 iterations per timestep.

The time variant lift, drag and moment coefficients and static pressure distribution for the airfoil are illustrated in Figure 5.8, together with the power spectral density variations of the same coefficients over logarithmic scale of frequency. The oscillating behavior in all of the coefficients indicates a probable buffet onset.

The peak point is measured at 34.3 Hz at the power spectral density variations of lift, drag, moment coefficients and static pressure and this frequency is determined as the buffet frequency at this analyzed condition.

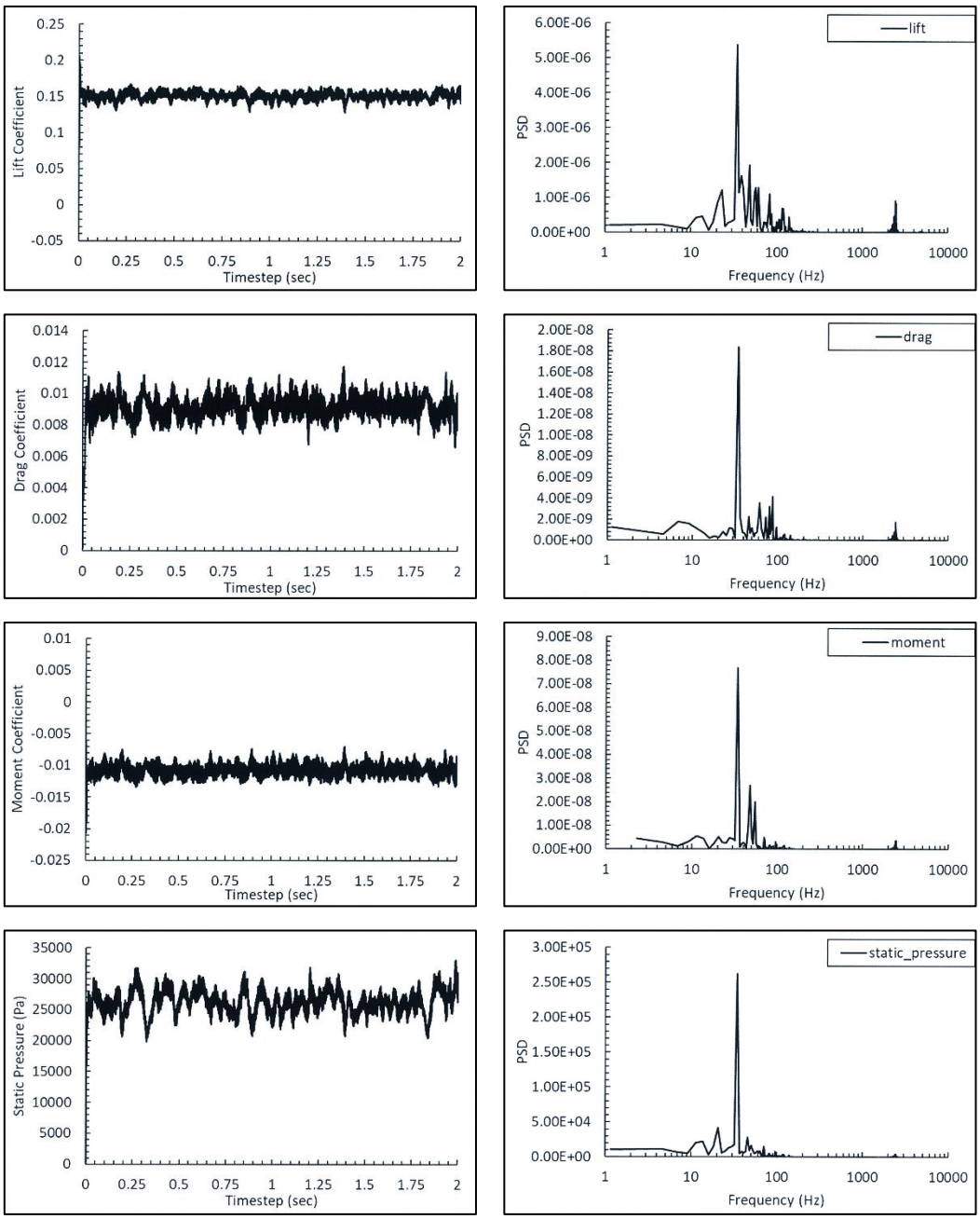

Figure 5.8. Lift, Drag, Moment Coefficient and Static Pressure Variation over Time and the Power Spectral Density Variations over Frequency at M0.775, α=4°, Re=4E+06

The buffet frequency of this flow condition is determined as 34.3 Hz based on the approach in the analysis of the previous flow condition. The numerical results cannot be compared with wind tunnel data for the current flow condition with low Reynolds number due to lack of wind tunnel data in terms of buffet frequency or Strouhal number.

The pressure and velocity u waveforms of the upper and lower surfaces of the airfoil at 50% and 80% of the chord is depicted in Figure 5.9. Between 50% and 80% of the chord, the oscillation frequency of the pressure waveforms increases at the upper surface, whereas it decreases at the lower surface when the flow approaches to the trailing edge. The oscillation characteristics of the pressure waveforms and u velocities are different than the ones at Dataset 4. The frequency and amplitude of the oscillations increase at 50% and 80% of the chord at upper surface and 50% of the chord at lower surface when the results are compared between Dataset 4 and Dataset 5. The change in the 80% of the chord at lower surface is not remarkable as other points.

The low frequency at the 50% of the chord and the higher frequency at the 80% of the chord on upper surface indicates that the shock oscillations start in a location after 50% of the chord. However, when the pressure and velocity u waveforms at 50% of the chord are compared, the ones at Dataset 5 are higher than Dataset 4. The probable reason is that the shock oscillations start in an earlier location than Dataset 4, which is closer to 50% of the chord. The oscillation frequencies at the lower surface are not quite different from each other, which indicates that oscillating shock does not exist at the lower surface.

Upper Surface:

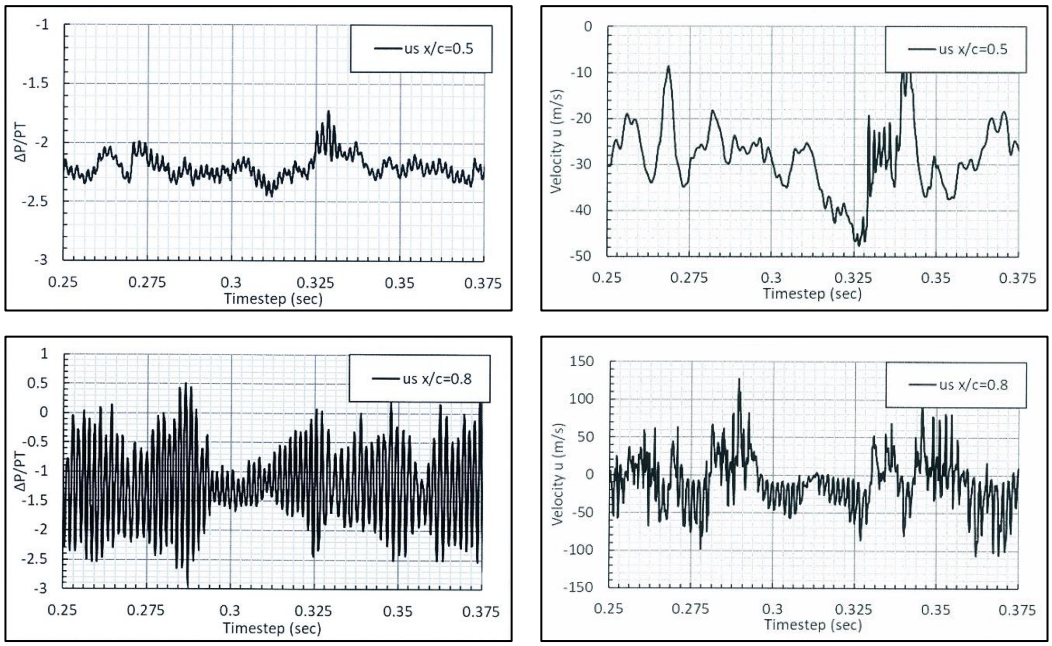

Lower Surface:

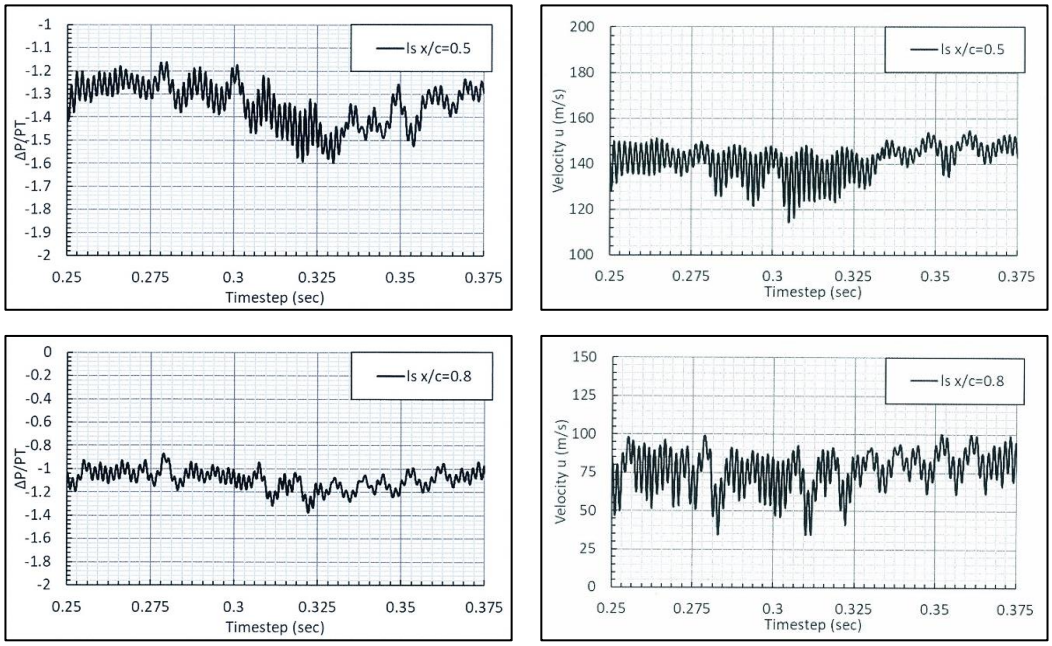

Figure 5.9. Comparison of Upper and Lower Surface Pressure and Velocity u Waveforms over Time at M0.775, α=4°, Re=4E+06

The pressure waveforms at 50% and 80% of the chord is stated at Figure 5.10. The oscillation frequency on the flow increases when it is moving from 50% of the chord to the 80% of the chord. Since the separation on the boundary layer due to the interaction with shock wave oscillation increases when the flow approaches to the trailing edge, the increase in the frequency is an expected result.

The comparative wind tunnel data for the same flow conditions are also stated in Figure 5.10 in orange color. The comparison of the numerical results with wind tunnel data shows that a serious difference is seen on the amplitudes of the oscillations of both results. On the contrary, the oscillation frequencies are similar. Since the flow around 50% and 80% of the chord is highly unstable and turbulent due to separated boundary layer region with vortices, the simulation of the subjected area is highly challenging. The amplitude and frequency of the oscillating pressure wave forms in this area can be simulated better with a higher mesh resolution and Detached Eddy Simulation. However, the simulation requires serious amount of computing power.

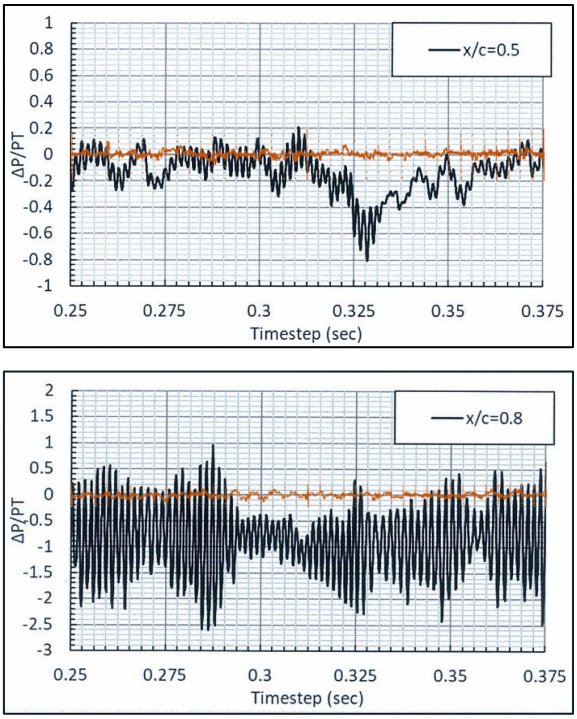

Figure 5.10. Pressure Waveforms over Time at M0.775, α=4°, Re=4E+06

The velocity u distribution over airfoil is stated as contour for various timesteps at one period in Figure 5.11. The oscillating behavior of the shock wave can be observed when the sub figures are examined with increasing timestep. The upper surface is subjected to oscillating shock at the critical Mach and Angle of Attack condition.

The frequency of the oscillating behavior of buffet is measured as 34.3 Hertz for the unsteady transient flow. The oscillation about 34.3 Hertz creates a Strouhal number as 0.17 at flow conditions of Dataset 5. A complete comparison cannot be made since there is no data with a low Reynolds number as in this analysis in wind tunnel results [2]. For the general comparison, the measured Strouhal number is relatively low from all of the values of the wind tunnel data, since the Strouhal numbers are stated for only high Reynolds number in wind tunnel results. In this manner, for the current flow conditions, the oscillating shock behavior exists; however, it is not obvious that the flow reaches the buffet onset.

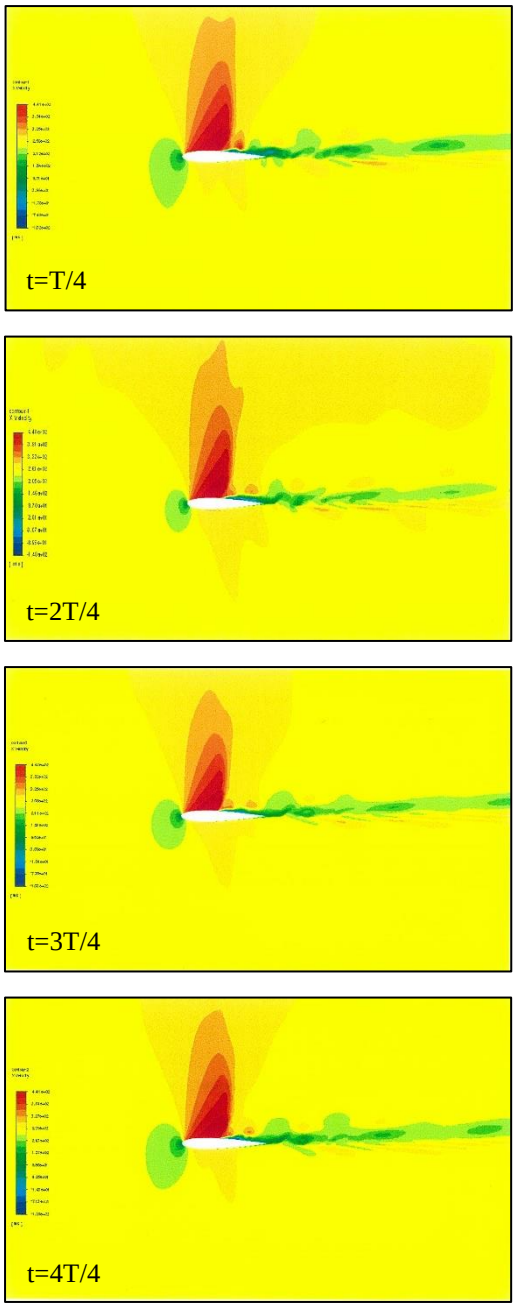

Figure 5.11. Velocity u Contour of Unsteady Analysis at Various Timesteps at M0.775, α=4°, Re=4E+06

The third analysis is conducted for M0.725 α=6° Re=4E+06. The steady transient analysis is conducted from the mesh configuration that has 428K mesh elements. The mesh optimization and the validation of the numerical results are stated in Section 4.4.2. The model is analyzed for 2 seconds with a 0.0001 second timestep. The residual tolerances are fixed to converge at least 10^{-6} up to 20 iterations per timestep.

The time variant lift, drag and moment coefficients and static pressure distribution for the airfoil are illustrated in Figure 5.12, together with the power spectral density variations of the same coefficients over logarithmic scale of frequency. the curves illustrate distinct oscillations indicating the buffet onset.

When the power spectral density variations of lift, drag, moment coefficients and static pressure are investigated, the peak point is measured at 36 Hz.

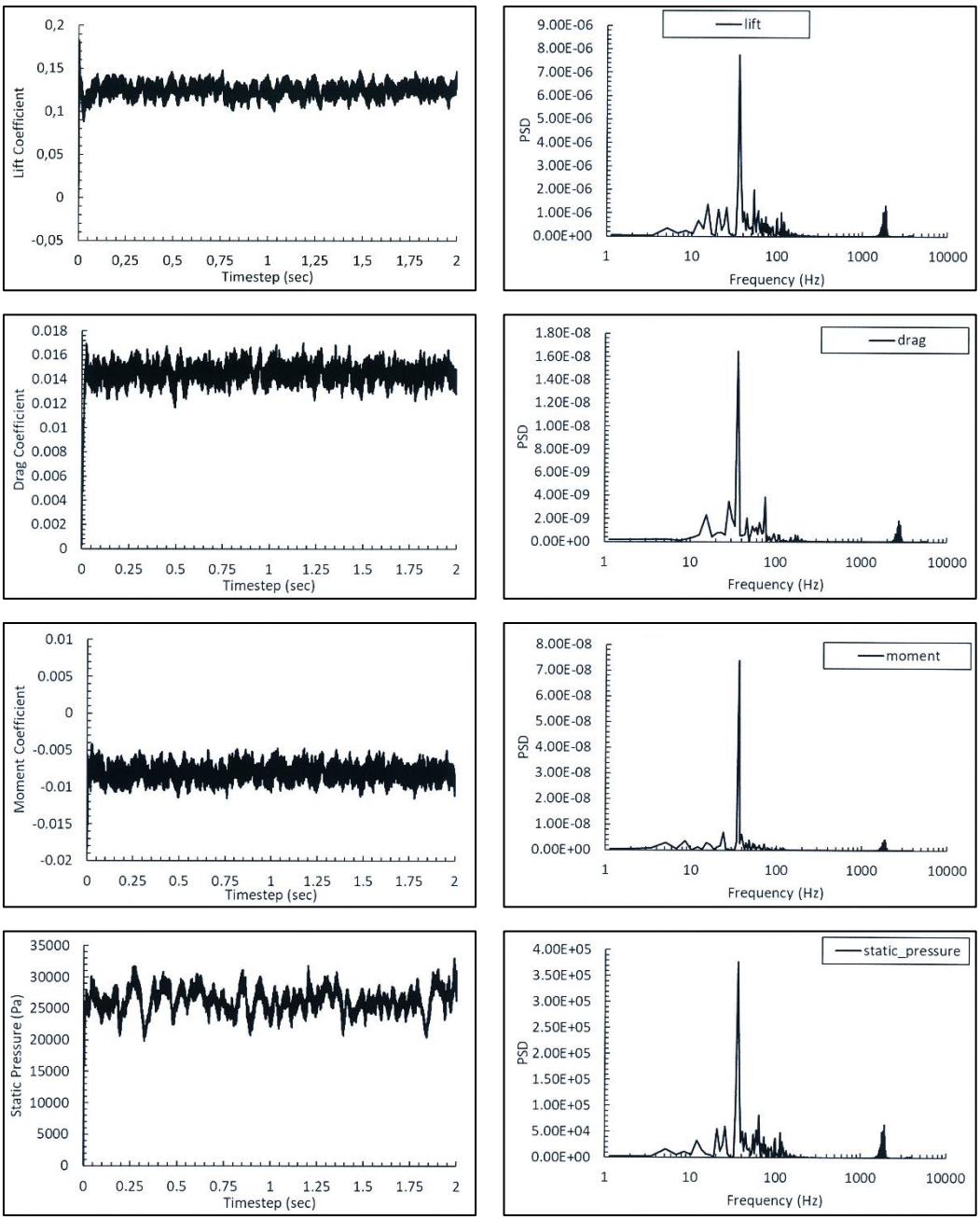

Figure 5.12. Lift, Drag, Moment Coefficient and Static Pressure Variation over Time and the Power Spectral Density Variations over Frequency at M0.725, α=6°, Re=4E+06

The dominant frequency of the flow is measured as 36 Hz and this is used as the buffet frequency for the condition. The numerical results cannot be compared with wind tunnel data for the current flow condition with low Reynolds number due to lack of wind tunnel data.

The pressure and velocity u waveforms of the upper and lower surfaces of the airfoil at 50% and 80% of the chord is depicted in Figure 5.13. It is seen from results that the frequency of the oscillations is distinctively higher at the upper surface then lower surface. In addition, the difference in the frequencies of the pressures and u velocities between 50% and 80% of the chord states that at the upper surface, the oscillation frequency increases when the flow approaches to the trailing edge. The amplitude of the oscillation at 50% of the chord of the upper surface highly increases at Dataset 6 flow conditions when compared to the ones in Dataset 4 and Dataset 5. The amplitudes of the oscillations of the lower surface pressure waveforms are similar to the ones in Dataset 5; however, the frequencies are different from each other in both flow conditions.

The high frequency values at both 50% and 80% of the chord upper surface indicates that the shock oscillations start in a location before 50% of the chord. The oscillation frequencies at the lower surface are not quite different from each other, which indicates that oscillating shock does not exist at the lower surface.

Upper Surface:

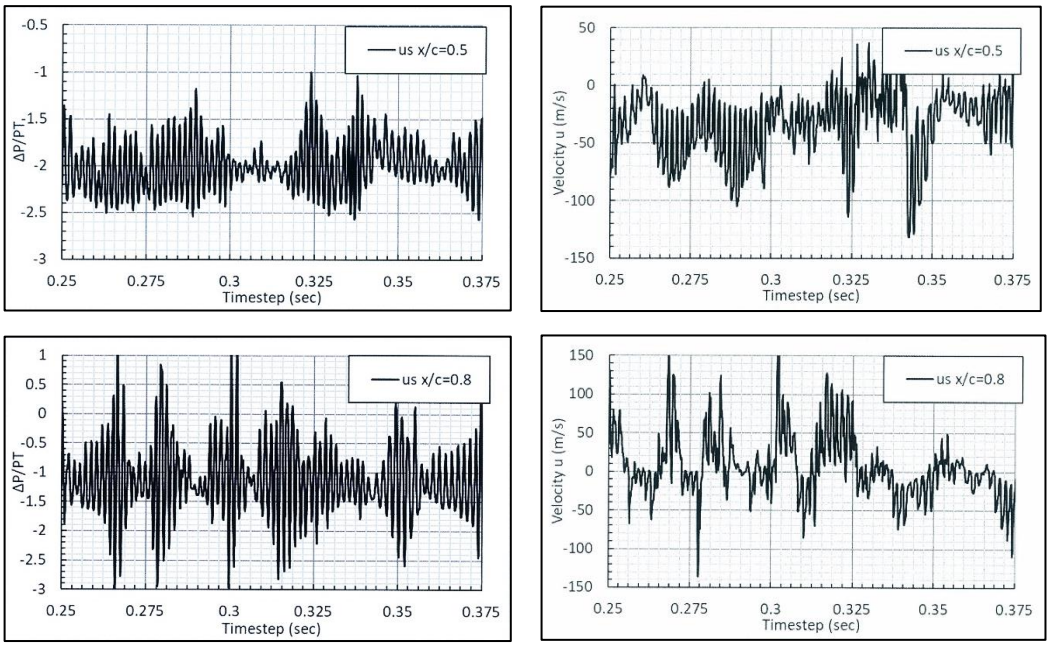

Lower Surface:

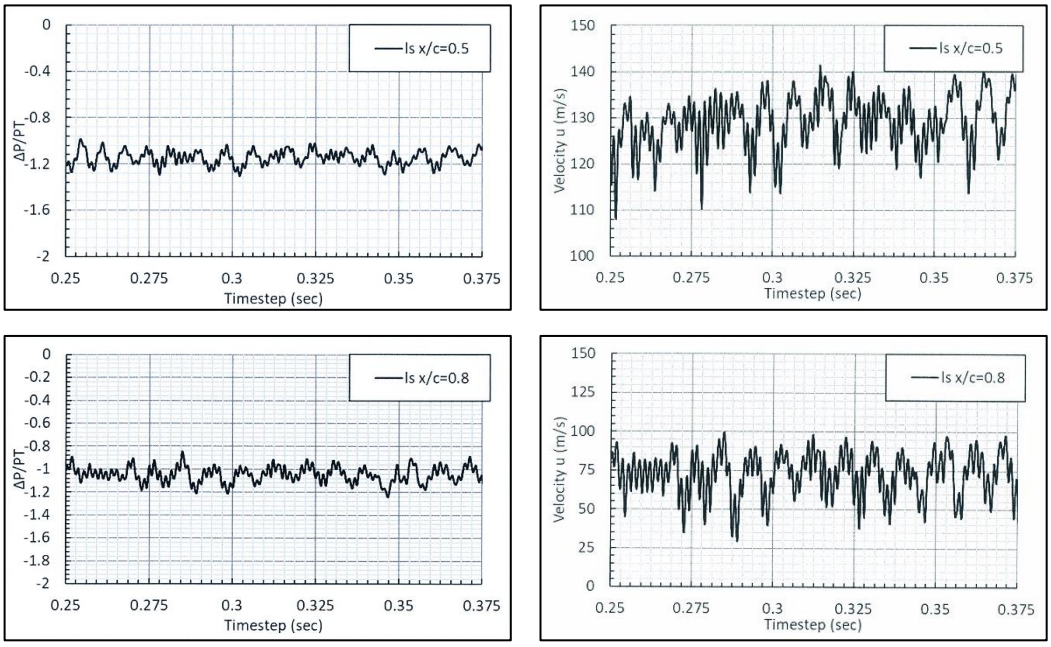

Figure 5.13. Comparison of Upper and Lower Surface Pressure and Velocity u Waveforms over Time at M0.725, α=6°, Re=4E+06

The pressure waveforms at 50% and 80% of the chord is stated at Figure 5.14. The oscillation frequency on the flow increases when it is moving from 50% to 80% of the chord, similar to the ones in Dataset 4 and Dataset 5.

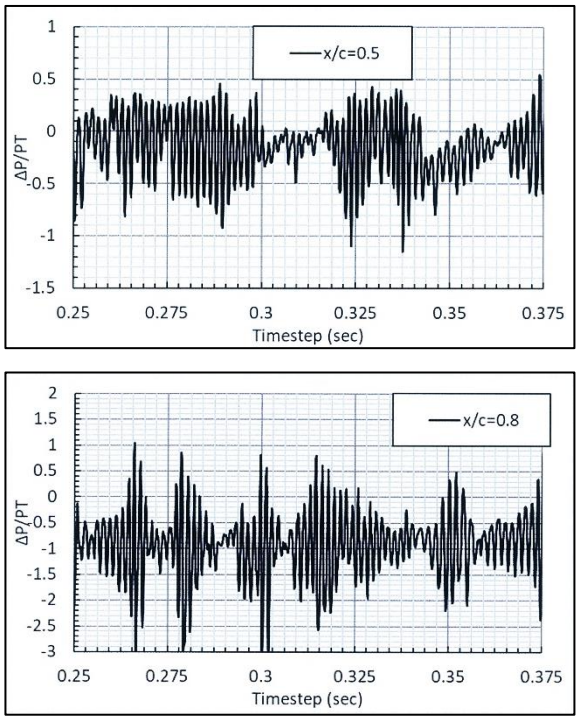

Figure 5.14. Pressure Waveforms over Time at M0.725, α=6°, Re=4E+06

The frequency of the oscillating behavior of buffet is measured as 36 Hertz for the unsteady transient flow. The oscillation about 36 Hertz creates a Strouhal number as 0.19. A complete comparison cannot be made since there are no data containing a low Reynolds number as in this analysis in wind tunnel results[2]. For the current flow conditions, the oscillating shock behavior exists; however, it is not obvious that the flow reaches the buffet onset.

Considering all three flow conditions that are analyzed with numerical solutions, it is seen that the frequency of the shock oscillations increases when the critical Mach number decreases. The possible reason behind this feature is that the shock location

moves downstream as the Mach number decreases. This leads to an increase distance on the chord which is subjected to oscillating shock with boundary layer interaction. As the distance which subjected to oscillation increases, the resultant oscillation frequency increases. It is also seen that the pressure and velocity u waveform characteristics of each location is highly different for all of the flow conditions. The variance at the frequencies of wavelengths indicates the starting location of the shock oscillations. The common characteristics for all flow conditions is that the flow reaches more unstable phase at the upper surface than lower surface. The probable reason is that in the steady results, the shock was observed on the upper surface for all three conditions.

5.3 Verification of the Numerical Analysis with Wind Tunnel Data

Since the unsteady shock wave oscillations are significantly observable for the conditions that have high Reynolds numbers [2], the verification of the unsteady transient flow is conducted on the similar flow conditions of unsteady transient analyses with Re=10E+06. In this manner, the flow conditions that are listed in Table 5.3 are analyzed for the verification of the buffet onset flow conditions at high Reynolds number in order to be consistent with the tested conditions are the wind tunnel as stated in [2]. The mesh resolution which is used at the verification of the steady analyses is basically kept the same as 428K elements, which is defined in detail in Section 4.4.2.

The verification of the transient unsteady flow with high Reynolds number is conducted with U-RANS equations with k-ω SST turbulence model. The results are compared for both simulation models and the wind tunnel dataset [2]. The model is analyzed for 2 seconds with a 0.0001 second timestep. The residual tolerances are fixed to converge at least 10^{-6} up to 20 iterations per timestep.

Table 5.3. *Analyzed Flow Conditions for High Reynolds Number* [2]

Dataset	***M***	***α (°)***	***Re***
Dataset 4	0.80	4	10E+06
Dataset 5	0.77	4	10E+06
Dataset 6	0.72	6	10E+06

The flow condition of the verification of the Dataset 4 at high Reynolds number is M0.8 α=4° Re=10E+06. The time variant lift, drag and moment coefficients and static pressure distribution for the airfoil are presented in Figure 5.15, together with the power spectral density variations of the same coefficients over logarithmic scale of frequency as well. The constant oscillated behavior of the flow is seen from lift, drag and moment coefficients and additionally, static pressure fluctuations. The first peak on the frequency around 0.1 seconds is due to the disturbance of the streamflow when it suddenly reaches the wing. The undamped oscillating behavior which is common in lift, drag, moment coefficient and static pressure variations over time is the evidence of a shock oscillation. It is also seen that the increase in the Reynolds number with the same flow conditions causes an increase in the frequency of the oscillations when Figure 5.5 and Figure 5.15 are compared with each other. The results are the evidence of the Reynolds number effect on the frequency characteristics of the buffet phenomenon.

When the power spectral density variations of lift, drag, moment coefficients and static pressure is investigated, the peak point is seen at 70.3 Hz on all four plots. The other bumps on the curve is due to the noise which is also seen in the variations of the coefficients and static pressure over time. When the results of the same flow conditions with different Reynolds numbers is compared with each other as in Figure 5.5 and Figure 5.15, it is seen that the dominant frequency is increasing when the Reynolds number of the condition increases.

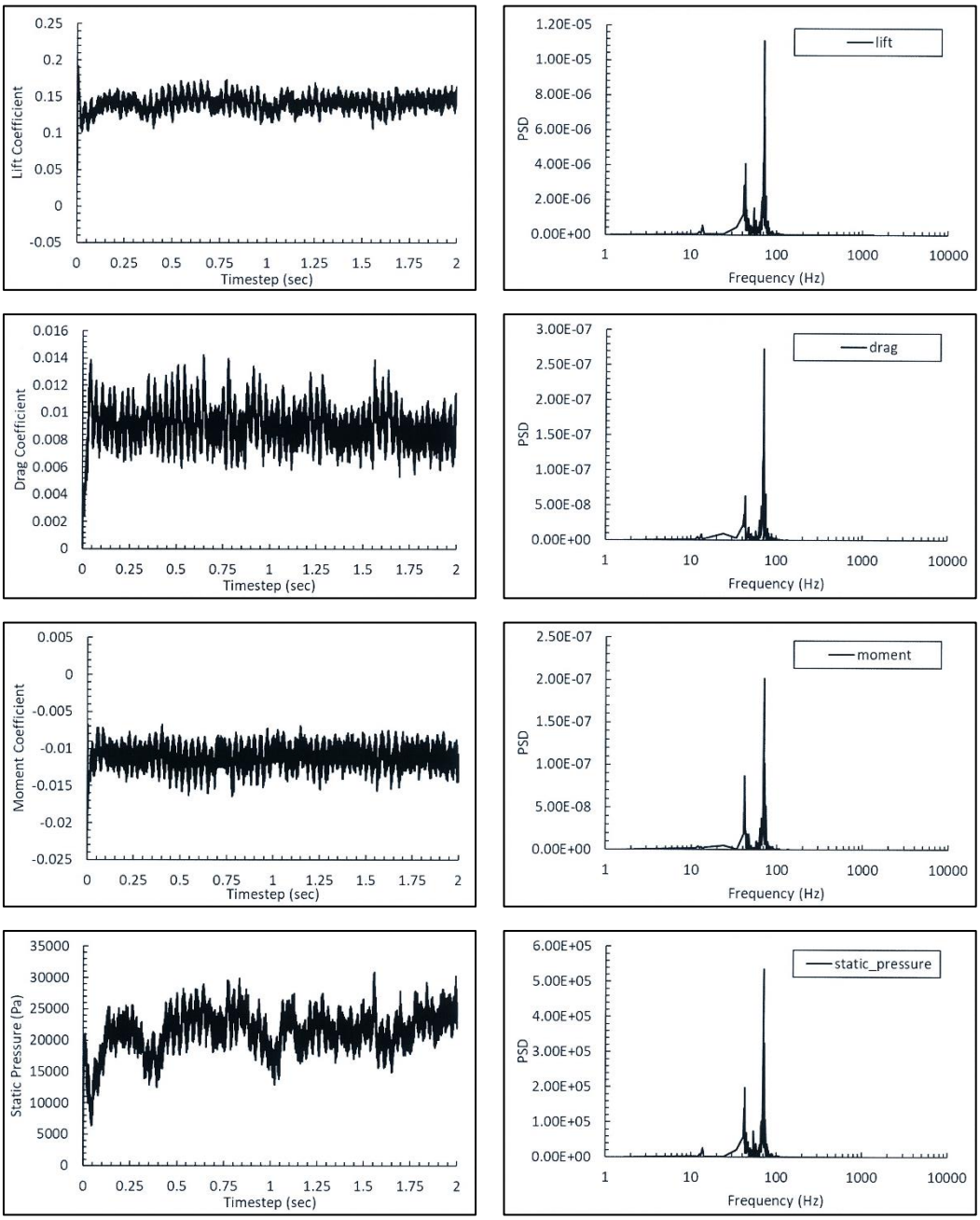

Figure 5.15. Lift, Drag, Moment Coefficient and Static Pressure Variation over Time and the Power Spectral Density Variations over Frequency at M0.80, α=4°, Re=10E+06

The dominant frequency of the flow is measured as 70.3 Hz for the condition and this is used as the buffet frequency at this flow condition. When the results of the numerical simulation and the wind tunnel data is compared, it is seen that the buffet frequency is measured as about 80 Hz at M0.8 α=4° Re=10E+06. The numerical results are not matched with wind tunnel data completely in this manner; however, it is seen that the similarity is high considering the relatively small difference between the frequencies.

The pressure and velocity u waveforms of the upper and lower surfaces of the airfoil at 50% and 80% of the chord is stated at Figure 5.16. It is seen from results that the frequency of the oscillations is higher at the upper surface then lower surface. In addition, as can be seen by the difference in the frequencies of the pressures and u velocities between 50% and 80% of the chord at the upper surface, the oscillation frequency increases when the flow approaches to the trailing edge. In the lower surface, it is seen that the frequency of the wavelengths at 50% of the chord is relatively higher than 80% of the chord. When the results are compared with the same versions with low Reynolds number, it is seen that the characteristics of the oscillations have changed. The amplitude and the frequency of the oscillations in each point increases with Reynolds number increase. The increase in the buffet frequency due to increase in Reynolds number is highly observable in pressure and velocity u waveform comparisons for both conditions.

Since the oscillation frequency increases abruptly from 50% to 80% of the chord at the lower surface, it can be concluded that the shock oscillation started in between 50% and 80% of the chord. The shock location is closer to the 50% of the chord since the oscillation frequency is higher at 50% of the chord when it is compared with the low Reynolds number condition of Dataset 4. The oscillation frequencies at the lower surface are not quite different from each other, which indicates that oscillating shock does not exist at the lower surface; however, the frequencies are distinctively larger than the low Reynolds number condition. The reason of this increase is the increase in the separation of the boundary layer at the lower surface.

Upper Surface:

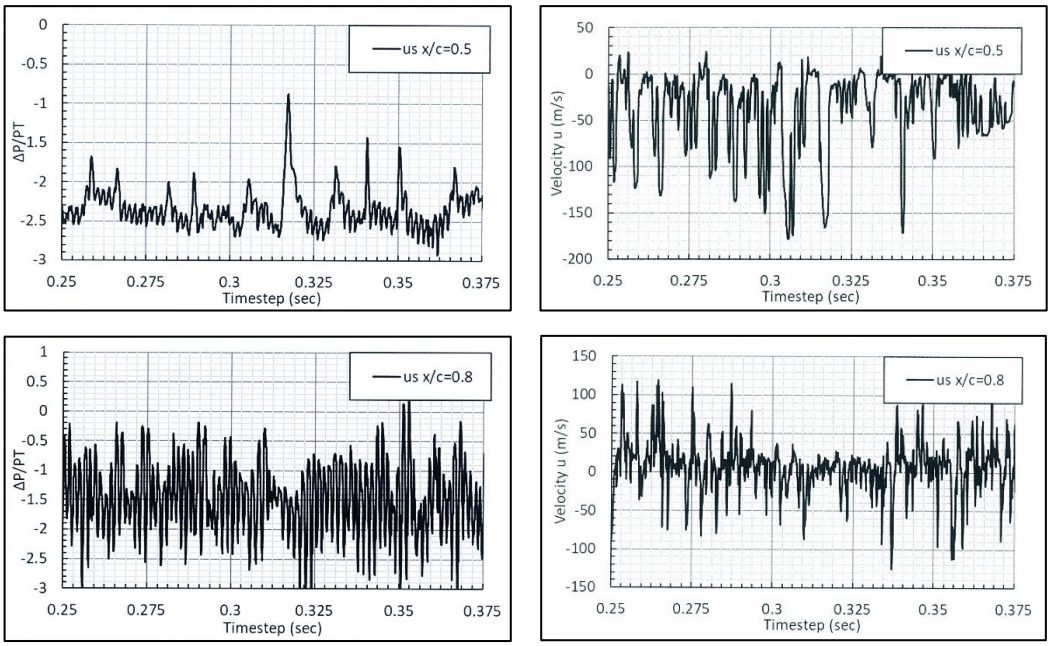

Lower Surface:

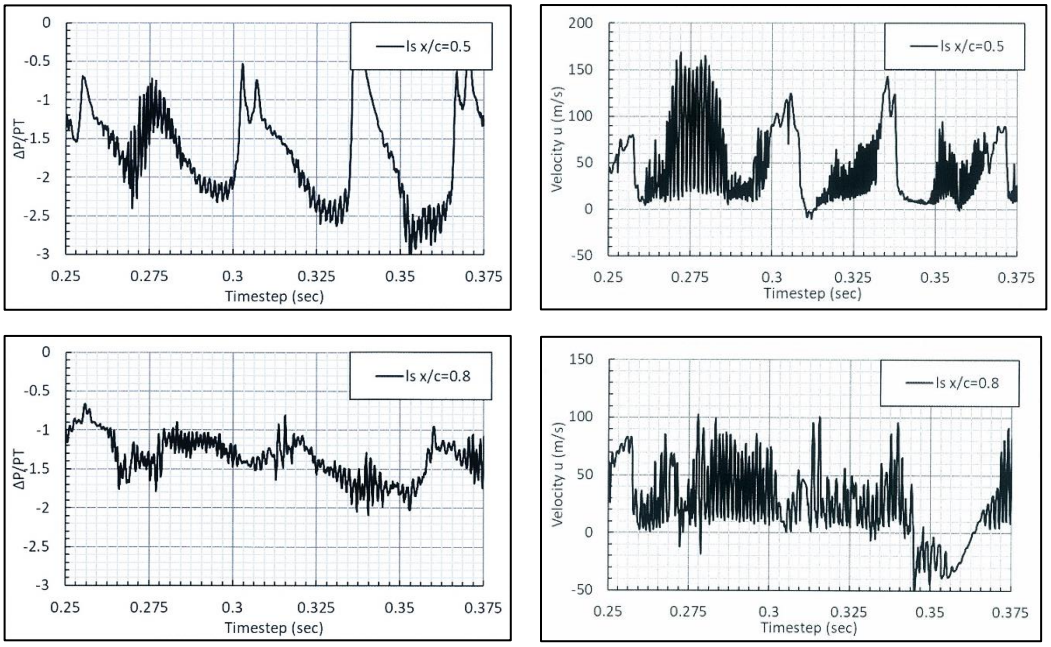

Figure 5.16. Comparison of Upper and Lower Surface Pressure and Velocity u Waveforms over Time at M0.80, α=4°, Re=10E+06

The pressure waveforms at 50% and 80% of the chord is stated at Figure 5.17. The oscillation frequency on the flow increases when it is moving from 50% of the chord to the 80% of the chord. Since the separation on the boundary layer due to the interaction with shock wave oscillation increases when the flow approaches to the trailing edge, the increase in the frequency is an expected result.

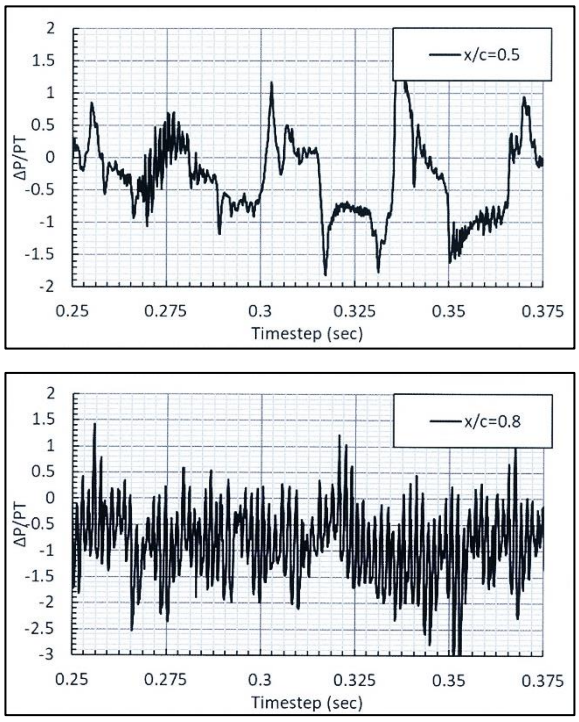

Figure 5.17. Pressure Waveforms over Time at M0.80, α=4°, Re=10E+06

The frequency of the oscillating behavior of buffet is around 29.7 Hertz for the low Reynolds number, the frequency increases up to 70.3 Hertz for the high Reynolds number. The results indicate that the increase in the Reynolds number causes a stronger separation when compared to the results with low Reynolds number.

The Strouhal number of the shock oscillation on the airfoil for M0.80 α=4° Re=10E+06 flow conditions are stated as 0.38 in the wind tunnel test results [2]. For the same flow conditions, Strouhal number is calculated as 0.33 from the numerical

solutions of U-RANS. The Strouhal number is basically the characteristics of the oscillated shock wave on the airfoil which is dependent to the flow conditions and geometry of the surface. In this manner, it is seen that the flow cannot be modeled accurately when looking at the mismatch on the Strouhal numbers of the two dataset; however, the model succeeded to converge to the wind tunnel data when looking at the 15% mismatch between two results. The location of the shock wave is predicted earlier than wind tunnel data with the steady numerical results and a similar mismatch occurs at transient results. Due to this reason, high mismatch is observed at the frequency and the Strouhal number of the buffet for this flow condition.

The same methodology for Dataset 4 is applied to the Dataset 5 and Dataset 6 in order to verify the numerical solution with wind tunnel data. U-RANS equations with k-ω SST turbulence model is used with the same convergence criteria and solution steps which are used during the analysis of Dataset 4. The results are verified with the wind tunnel dataset as stated in [2].

For the verification of the results of Dataset 5, the closest wind tunnel data to the flow condition of M0.77 α=4° Re=10E+06 that has been stated in Table 5.3 is analyzed.

The time variant lift, drag and moment coefficients and static pressure distribution for the airfoil is stated in Figure 5.18, together with the power spectral density variations of the same coefficients over logarithmic scale of frequency as well. the increase in Reynolds number at this flow conditions of Dataset 5 causes an increase in the buffet frequency, similar to the results on Dataset 4.

When the power spectral density variations of lift, drag, moment coefficients and static pressure is investigated, the peak point is seen at 82.6 Hz on all four plots. When the results of the same flow conditions with different Reynolds numbers is compared with each other as in Figure 5.8 and Figure 5.18, it is seen that the dominant frequency is increasing when the Reynolds number of the condition increases.

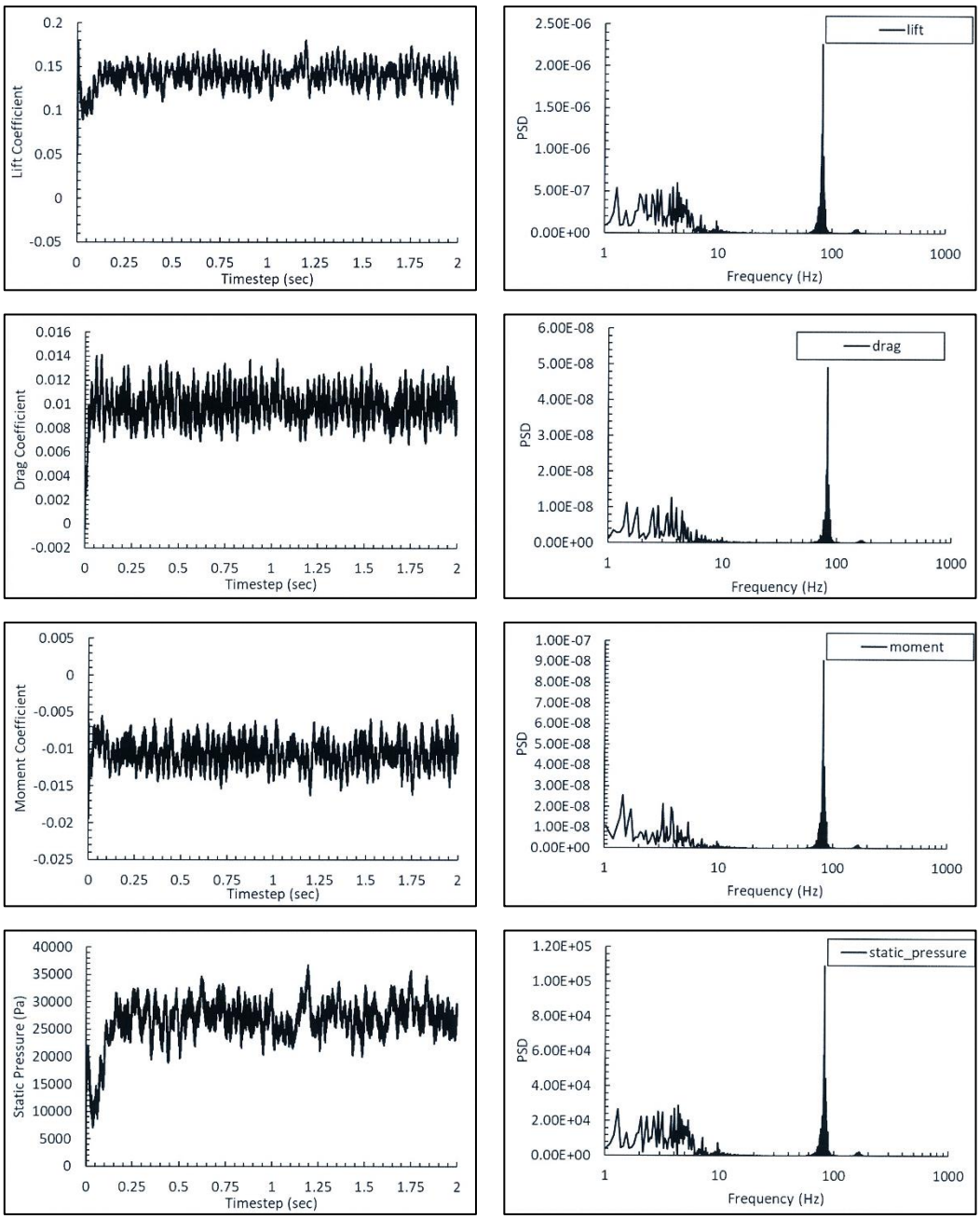

Figure 5.18. Lift, Drag, Moment Coefficient and Static Pressure Variation over Time and the Power Spectral Density Variations over Frequency at M0.77, α=4°, Re=10E+06

The dominant frequency of the flow is measured as 82.6 Hz for the condition and this is used as the buffet frequency for this flow condition. The buffet frequency is stated as about 92 Hz at M0.77 α=4° Re=10E+06 in wind tunnel results [2]. The numerical results are not matched with wind tunnel data completely in this manner; however, it is seen that the similarity is high considering the relatively small difference between the frequencies.

The pressure and velocity u waveforms of the upper and lower surfaces of the airfoil at 50% and 80% of the chord is stated at Figure 5.19. The frequency of the oscillations is higher at the upper surface then lower surface, similar with the results in Dataset 4. In addition, as can be seen by the difference in the frequencies of the pressures between 50% and 80% of the chord, the oscillation frequency increases when the flow approaches to the trailing edge. The comparison of the same flow condition with low and high Reynolds numbers indicates that the oscillation frequencies of the pressure and velocity u increase in all points. The amplitudes of the oscillations increase at 80% of the chord; however, they decrease at the 50% of the chord.

The increase in the oscillation frequency from 50% to 80% of the chord indicates the shock wave oscillations starts in a location between 50% and 80% of the chord, closer to 50% of the chord. The oscillation frequencies at the lower surface also increases from 50% to 80% of the chord, which indicates the increase of separation at the boundary layer.

Upper Surface:

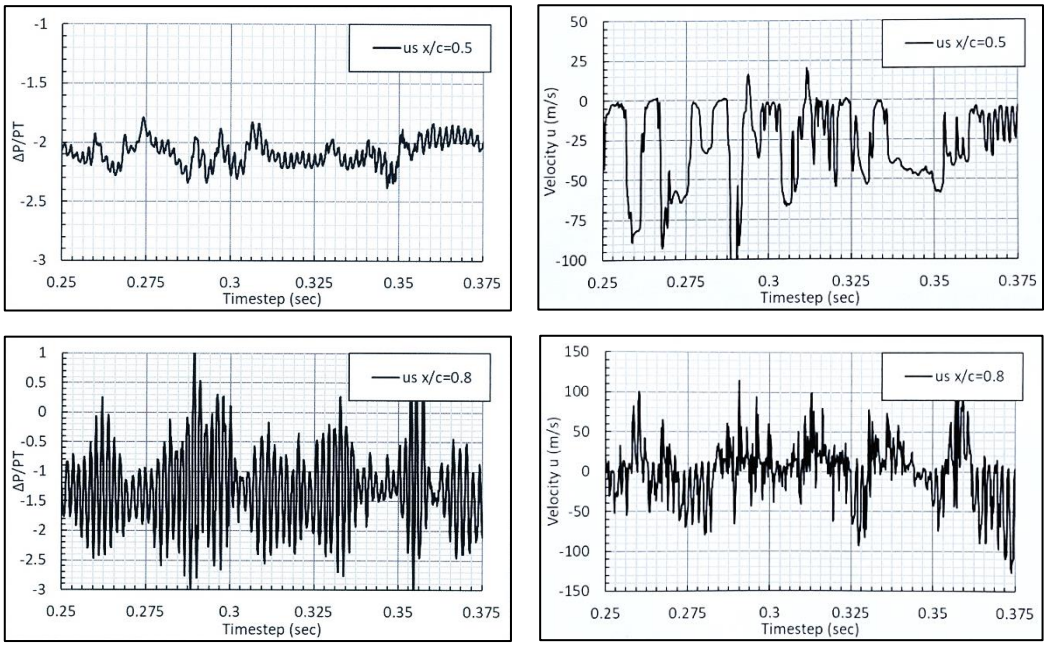

Lower Surface:

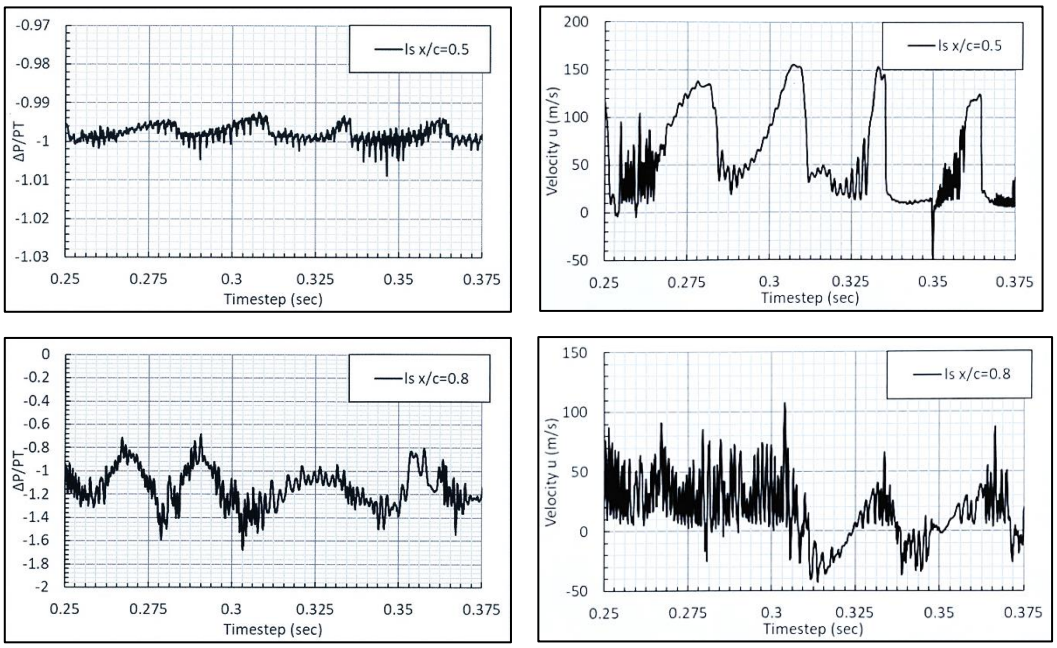

Figure 5.19. Comparison of Upper and Lower Surface Pressure and Velocity u Waveforms over Time at M0.77, α=4°, Re=10E+06

The pressure waveforms of the at 50% and 80% of the chord is stated at Figure 5.20. The oscillation frequency on the flow increases when it is moving from 50% of the chord to the 80% of the chord.

The comparative wind tunnel data for the same flow conditions are also stated in Figure 5.20 in orange color. The comparison of the numerical results with wind tunnel data shows that a serious difference is seen on the amplitudes of the oscillations of both results. On the contrary, the oscillation frequencies are similar. Since the flow around 50% and 80% of the chord is highly instable and turbulent due to separated boundary layer region with vortexes, the simulation of the subjected area is highly challenging. The amplitude and frequency of the oscillating pressure wave forms in these area can be simulated better with a higher mesh resolution and Detached Eddy Simulation. However, the simulation requires serious amount of computing power.

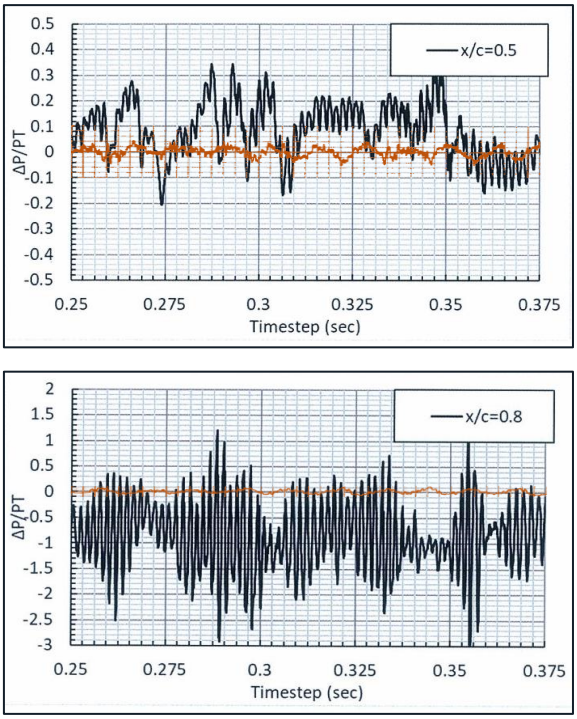

Figure 5.20. Pressure Waveforms over Time at M0.77, α=4°, Re=10E+06

The velocity u distribution over airfoil is stated as contour for various timesteps at one period in Figure 5.21. The oscillating behavior of the shock wave can be observed when the sub figures are examined with increasing timestep. The upper surface is subjected to oscillating shock at the critical Mach and Angle of Attack condition. The comparison between Figure 5.11 and Figure 5.21 shows that the rank in separation at the boundary layer and the shock wave oscillation characteristics differs as the Reynolds number increase for the same flow condition.

The frequency of the buffet is measured as around 34.3 Hertz for low Reynolds number, the frequency increases up to 82.6 Hertz for the high Reynolds number. The results indicate that the increase in the Reynolds number causes an increase in the oscillation frequency at the trailing edge.

The Strouhal number for M0.77 α=4° Re=10E+06 flow conditions is stated as 0.45 in the wind tunnel test results [2]. For the same flow conditions, Strouhal number is calculated as 0.40 from the numerical solutions. The flow cannot be modeled accurately when looking at the mismatch on the Strouhal numbers of the two data. However, the model succeeded to converge to the wind tunnel data when looking at the 13% mismatch.

The frequency and the Strouhal number of the buffet cannot be matched and verified with wind tunnel data. However, the increase in the frequency of the shock oscillation is observed and the results approach the wind tunnel data. The possible reason behind this mismatch is that the mesh resolution is not satisfactory for the simulation of all the shock wave oscillations and the separations around boundary layer.

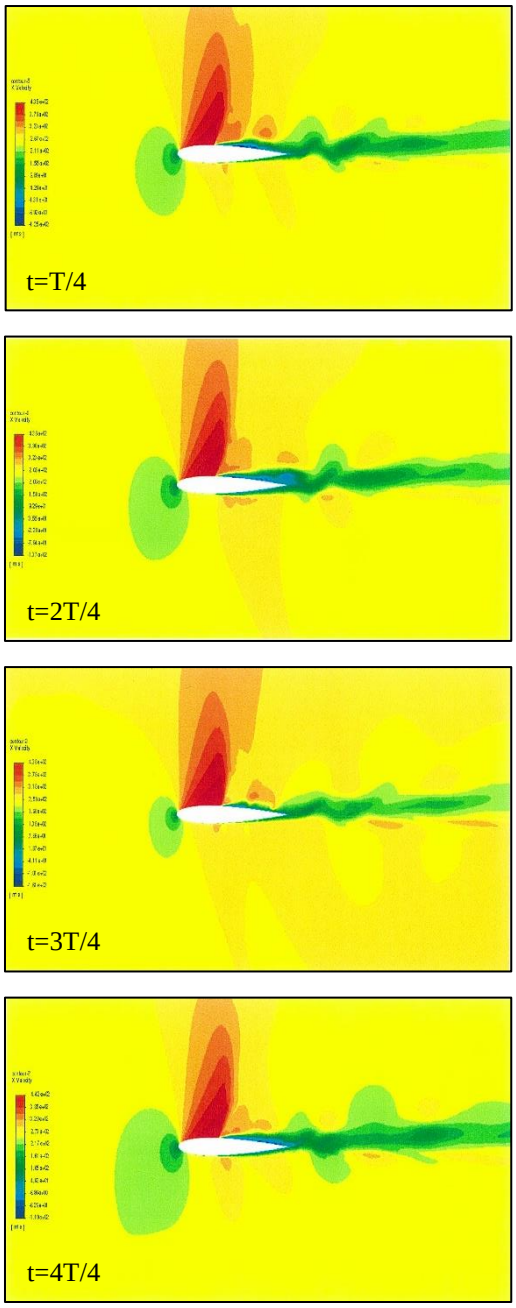

Figure 5.21. Velocity u Contour of Unsteady Analysis at Various Timesteps at M0.77, α=4°, Re=10E+06

For the verification of the results of Dataset 6, the closest wind tunnel data to the flow condition of M0.72 α=6° Re=10E+06 that has been stated in Table 5.3 is analyzed.

The time variant lift, drag and moment coefficients and static pressure distribution for the airfoil is stated in Figure 5.22, together with the power spectral density variations of the same coefficients over logarithmic scale of frequency as well. The frequency of the oscillation increases due to the increase in Reynolds number, similar to the results in Dataset 4 and Dataset 5. When the power spectral density variations of lift, drag, moment coefficients and static pressure is investigated, the peak point is seen at 97.6 Hz on all four plots.

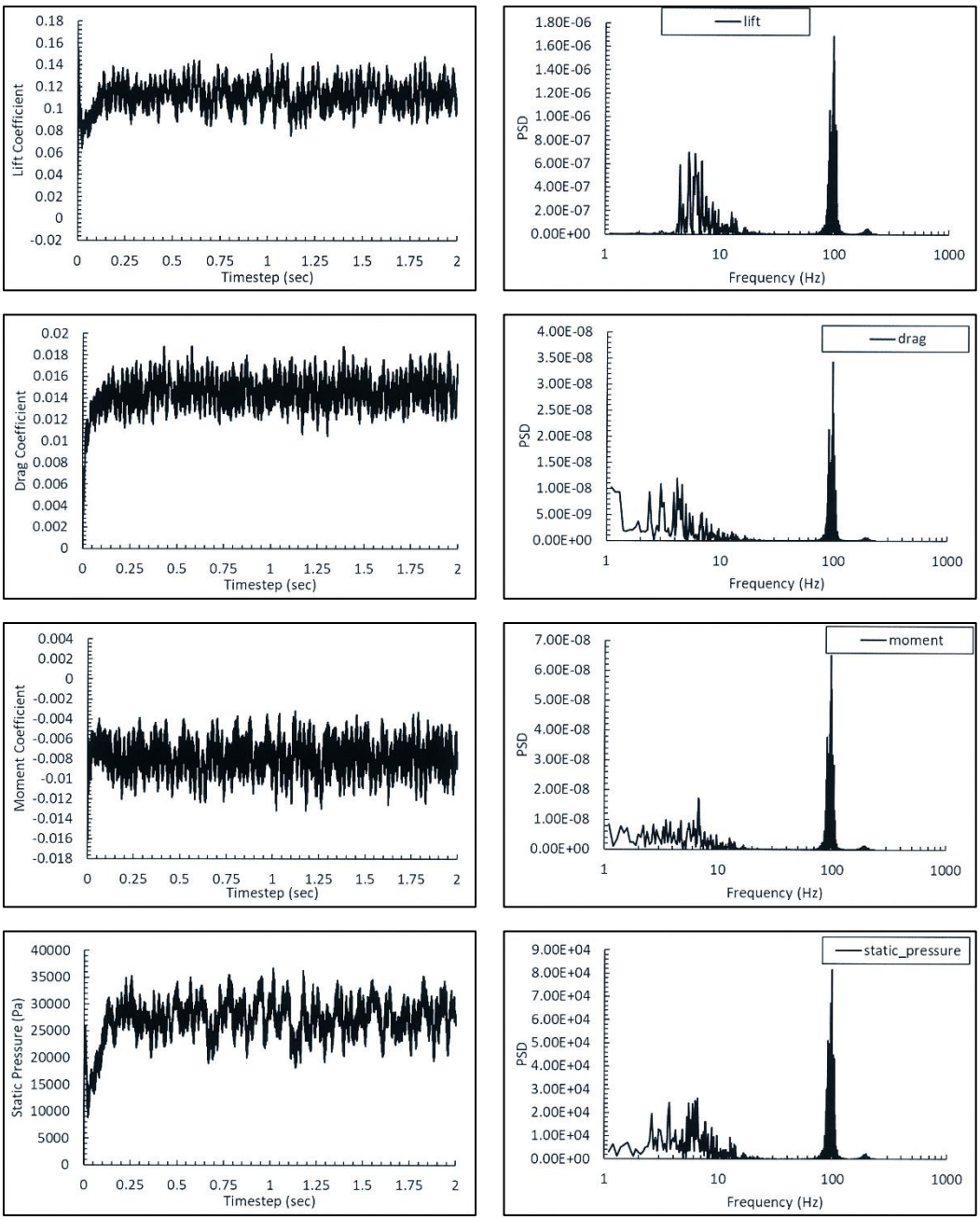

Figure 5.22. Lift, Drag, Moment Coefficient and Static Pressure Variation over Time and the Power Spectral Density Variations over Frequency at M0.72, α=6°, Re=10E+06

The dominant frequency of the flow is measured as 97.6 Hz for the condition and this is used as the buffet frequency for this flow condition. The buffet frequency is stated as about 106 Hz at M0.72 α=6° Re=10E+06 in wind tunnel data. The numerical results are not matched with wind tunnel data completely in this manner; however, it is seen that the similarity is high considering the relatively small difference between the frequencies.

The pressure and velocity u waveforms of the upper and lower surfaces of the airfoil at 50% and 80% of the chord is stated at Figure 5.23. It is seen from results that the frequency of the oscillations is higher at the upper surface then lower surface. The increase in Reynolds number leads to increase in both frequency and the amplitude of the wavelengths of all four points.

The high frequency values at both 50% and 80% of the chord upper surface indicates that the shock oscillations start in a location before 50% of the chord. The difference at the frequencies between 50% and 80% of the chord is due to the boundary layer separation occurs at near trailing edge.

Upper Surface:

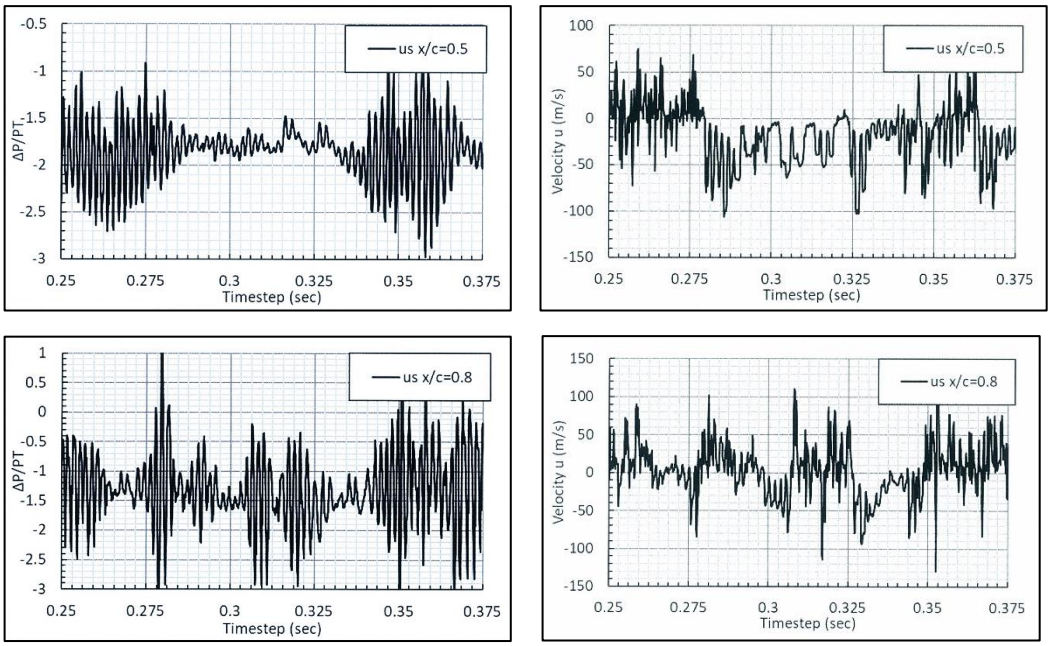

Lower Surface:

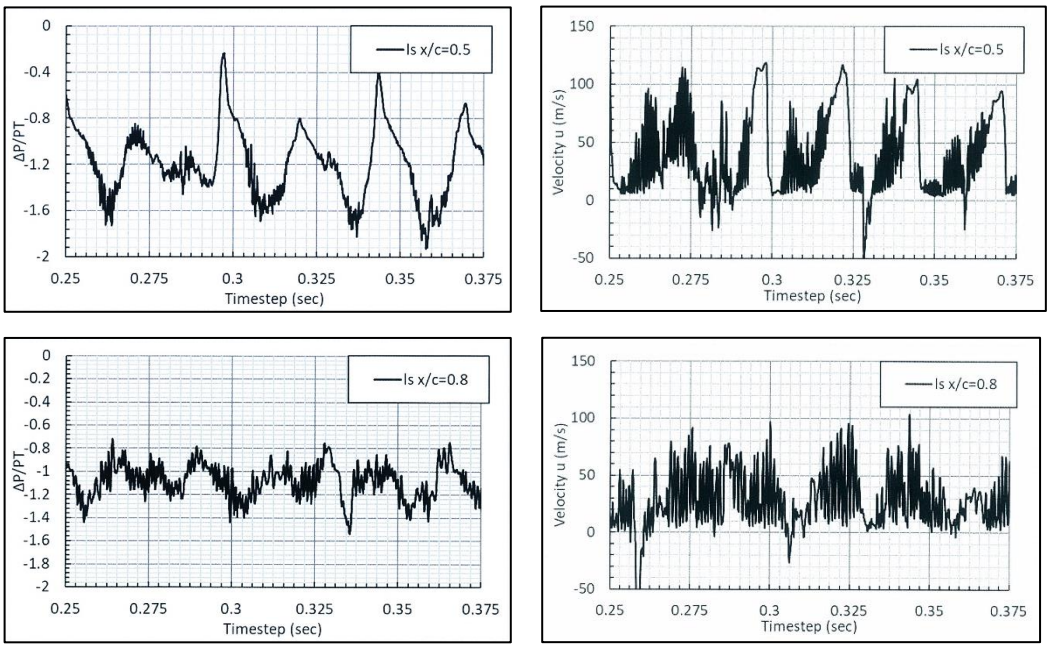

Figure 5.23. Comparison of Upper and Lower Surface Pressure and Velocity u Waveforms over Time at M0.72, α=6°, Re=10E+06

The pressure waveforms at 50% and 80% of the chord is stated at Figure 5.24. The oscillation frequency on the flow increases when it is moving from 50% of the chord to the 80% of the chord, similar to the results of Dataset 4 and Dataset 5.

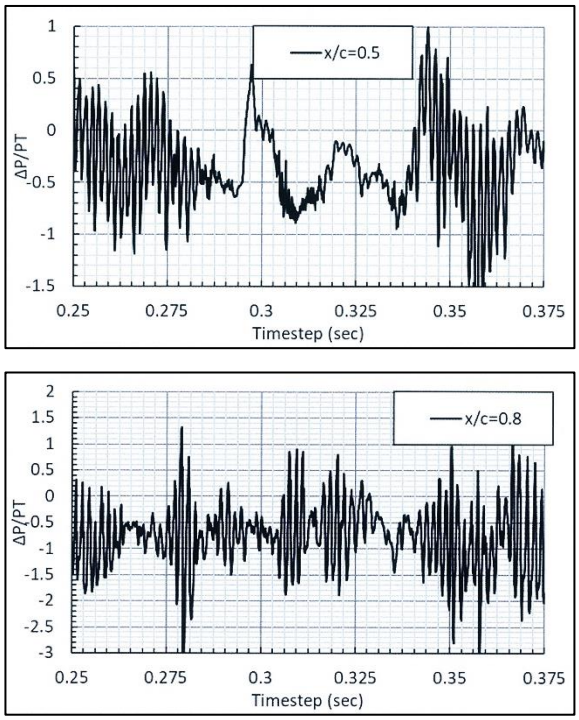

Figure 5.24. Pressure Waveforms over Time at M0.72, α=6°, Re=10E+06

The Strouhal number for M0.72 α=6° Re=10E+06 flow condition is stated as 0.55 in the wind tunnel test results [2]. For the same flow conditions, Strouhal number is calculated as 0.51 from the numerical solutions. It is seen that the flow cannot be modeled accurately when looking at the mismatch on the Strouhal numbers of the two data. On the contrary, the flow conditions are modeled with high accuracy when looking at the 8% mismatch between two results. the possible way of increasing the accuracy of the numerical solution is increasing the mesh quality and modeling the flow with Detached Eddy Simulation.

Considering all three flow conditions that are analyzed with numerical solutions, it is seen that the frequency of the shock oscillations increases when the critical Mach number decreases. The possible reason behind this feature is the same with the low Reynolds number conditions. It is also seen that the pressure waveform characteristics of each location is highly different for all of the flow conditions. The common characteristics for all flow conditions is that the flow reaches more unstable phase at the upper surface than lower surface. It is also seen that the frequency of the oscillations increases when the Reynolds number increases, and the buffet frequency is better observed from the Strouhal numbers.

The fluctuations in the moment coefficient affects the stability behavior. This kind of frequent oscillations on the wing as seen in all moment results stimulate the short period oscillation of the aircraft. The short period oscillations are highly critical for the augmented fighter type aircrafts since the short period characteristics defines the time to double amplitude and the time to double amplitude purely defines the instability limitations of the aircraft [44]. As the characteristics of the moment coefficient oscillations have been examined, it is seen that the shock oscillations of buffet can be an additional criterion for the definition of the instability limit of the aircraft since the frequency of the oscillations of the moment coefficient of the airfoil are high enough to be able to stimulate the short period characteristic. It is also seen that, especially at high Reynolds numbers, the frequency of the oscillations increases and the higher the frequency becomes even more critical as the effect of the increase in the oscillation on the instability limit increases even more.

CHAPTER 6

CONCLUSIONS

6.1 Concluding Remarks

The buffet onset characteristics of the NACA0012 airfoil is investigated through several conditions with the commercial computational fluid dynamics tool as ANSYS Fluent and the results are verified with wind tunnel test data in this study. The study first investigates steady conditions through pressure coefficient distributions. The mesh independency and turbulence model that is suitable for the analysis of the unsteady characteristics of the buffet is investigated for the several mesh and turbulence models. The results are closely matched with wind tunnel data with the k-ω SST turbulence model. The pressure coefficient distribution is predicted as coherent with the wind tunnel data and the location of the shock wave and pressure drop on both upper and lower surfaces of the airfoil are predicted fairly accurately. The k-ε and Spalart-Allmaras models have also a close match with the pressure coefficient distribution especially before the shock location. However, the shock location is predicted upstream of the location of the wind tunnel results with the Spalart-Allmaras and downstream the real value with k-ε turbulence model. k-ω SST turbulence model is especially successful at predicting the shock wave location around upper and lower surfaces of the airfoil. The steady analyses are verified with the wind tunnel test results for two different Reynolds numbers. As the Reynolds number increases, the shock wave oscillations during buffet is highly observable and predictable, the high Reynolds number is preferred for the verification. The numerical results for the low Reynolds number is highly compatible with wind tunnel results. However, for the high Reynolds number, the shock wave is predicted upstream of the true location when compared to the wind tunnel data for one flow

condition. The other two flow conditions are predicted with high accuracy, in terms of both pressure distributions and the shock wave location. The difference between numerical solution and wind tunnel results could originate from several reasons; however, it should be considered that there is a significant increase in the Reynolds number of the analyzed condition which is from 3.7E+06 to 10E+06. The prediction of the shock wave with such high Reynolds number can be a challenge for computational methods even in two dimensional analyses.

The steady and unsteady transient analyses are conducted after the verification of the steady analyses. The steady flow around airfoil before the buffet onset is investigated with transient analyses. It is identified that no oscillation occurs on the shock wave at upper and lower surfaces of the airfoil after the flow is settled on the geometry. The flow is settled after 0.25 seconds and the steady flow can be seen clearly from pressure distributions. The unsteady shock oscillated flow characteristics is investigated through unsteady transient analyses. The angle of attack of the steady analyses are conducted with approximately 2-degree increment for the unsteady analyses. The analysis results have shown that after the buffet onset the shock oscillation continues with nearly constant bandwidth after the flow is settled. The oscillating characteristics of the shock wave can be seen on the pressure distributions. The drag and lift coefficient distributions over time also indicated the oscillating behavior of the shock wave. The Strouhal numbers of the unsteady transient flow with low Reynolds number might seem less to trigger buffet; however, the flow conditions are for the low Reynolds number. It is obvious that the increase in the Reynolds number would lead to higher oscillations on the airfoil with the same flow conditions. Indeed, the verification results of the unsteady transient flow have shown that the oscillations of the shock wave are highly increased. The resultant Strouhal numbers for high Reynolds number highly compatible with the wind tunnel data.

The overall investigation of the buffet onset on two dimensional airfoil analyses have shown that the shock oscillation is highly dependent on Mach number, angle of attack and Reynolds number. The critical Mach number for the transonic buffet is

reached at the transonic flow condition at a specific angle of attack. The relation between Mach number and the angle of attack is inversely proportional. As the Mach number is increased, the angle of attack that triggers buffet starts to decrease. The Reynolds number increase directly affects the buffet characteristics. As the Reynolds number for the flow condition increases, the oscillation of the shock wave increases, which provides basis for reaching the critical bandwidth for the buffet.

6.2 Future Work

The investigation of the buffet onset on two dimensional flow is the fundamental step through understanding of the basic characteristics of the oscillating behavior of the flow on buffet phenomenon. The turbulent, unsteady behavior of the flow at high Reynolds numbers with critical Mach and angle of attack conditions is a challenging case for the modelling of buffet characteristics on the airfoil even in two dimensional motion. Since the analyses are conducted for a limited computational power, the verification and transient analyses will be enhanced with the use of a computer of increased processor and memory. After investigation of the NACA0012 airfoil buffet onset characteristics, it is crucial for investigation of an alternative airfoil profile for the further analyses.

REFERENCES

[1] B.H.K. Lee, "Oscillatory shock motion caused by transonic shock boundary-layer interaction," *J. AIAA.*, vol. 28, no. 5, 1990, pp. 942–944.

[2] J.B. McDevitt, A.F. Okuno, "Static and dynamic pressure measurements on a naca0012 airfoil in the ames high reynolds number facility," in *Tech. Paper NASA TP-2485, National Aeronautics and Space Administration*, 1985.

[3] W.F. Hilton and R.G. Fowler, "Photographs of shock wave movement," in *Tech. Paper NPL R&M No. 2692, National Physical Laboratories*, 1947.

[4] D.G. Mabey, "Oscillatory flows from shock induced separations on biconvex aerofoils of varying thickness in ventilated wind tunnels," in *Tech. Paper AGARD CP-296, Boundary layer effects on unsteady airloads*, Aix-en-Provence, France, 1981, pp. 1–14.

[5] H.H. Pearcey, "Some effects of shock-induced separation of turbulent boundary layers in transonic flow past aerofoils," in *Tech. Paper ARC R&M-3108, Aeronautical Research Council*, 1955.

[6] H.H. Pearcey, "A method for the prediction of the onset of buffeting and other separation effects from wind tunnel tests on rigid models," *AGARD TR 223, National Physics Laboratory*, 1958.

[7] J.D. Crouch, A. Garbaruk, D. Magidov, A. Travin, "Origin of transonic buffet on aerofoils," *J. Fluid Mech.*, 2009, pp. 357–369.

[8] H. Tijdeman, "Investigations of the transonic flow around oscillating Airfoils," Ph. D. dissertation, Delft Univ. Technology, TU Delft, 1977.

[9] B.H.K. Lee, "Self-Sustained shock oscillations on airfoils at transonic speeds," in *Prog. Aerosp. Sci.*, 2001.

[10] S. Raghunathan, R.D. Mitchell, M.A. Gillan, "Transonic shock oscillations on NACA0012 aerofoil," *J. Shock Waves*, 1998, pp. 191–202.

[11] J.B. McDevitt, L.L. Levy Jr., G.S. Deiwert, “Transonic flow about a thick circular-arc airfoil,” *J. AIAA*, 1976, pp. 606–613.

[12] J.B. McDevitt, “Supercritical flow about a thick circular-arc airfoil,” in *Tech. Paper NASA-TM 78549, National Aeronautics and Space Administration*, 1979.

[13] B.H.K. Lee, “Investigation of flow separation on a supercritical airfoil,” *J. Aircr.*, 1989, pp. 1032–1037.

[14] B.H.K. Lee, F.A. Ellis, J. Bureau, “Investigation of the buffet characteristics of two supercritical airfoils,” *J. Aircr.*, 1989, pp. 731–736.

[15] J. Dandois, P. Molton, A. Lepage, A. Geeraert, V. Brunet, J.B. Dor, et al, “Buffet characterization and control for turbulent wings,” in *Tech. Paper AerospaceLab*, 2013, pp. 1–17.

[16] L. Jacquin, P. Molton, S. Deck, B. Maury, D. Soulevant, “Experimental study of shock oscillation over a transonic supercritical profile,” *J. AIAA*, 2009, pp. 1985–1994.

[17] L. Jacquin, P. Molton, S. Deck, B. Maury, D. Soulevant, “An experimental study of shock oscillation over a transonic supercritical profile,”in *Proc. 35th AIAA Fluid Dynamics Conference and Exhibit*, Toronto, Ont., 2005.

[18] S. Deck, “Numerical simulation of transonic buffet over a supercritical airfoil,” *J. AIAA*, 2005, pp. 1556–1566.

[19] J.D. Crouch, A. Garbaruk, D. Magidov, L. Jacquin, “Global structure of buffeting flow on transonic airfoils,” in *IUTAM Symp. Unsteady Separated Flows and Their Control*, Springer, 2009.

[20] M. Thiery, E. Coustols, “URANS computations of shock-induced oscillations over 2d rigid airfoils: influence of test section geometry,” *J. Flow, Turbul. Combust.*, 2005, pp. 331–354.

[21] N.F. Giannelis, G.A. Vio, “Aeroelastic interactions of a supercritical aerofoil in the presence of transonic shock buffet,” in *Proc. 54th AIAA Aerospace Sciences Meeting*, San Diego, CA, 2016.

[22] J.D. Crouch, A. Garbaruk, D. Magidov, “Predicting the onset of flow unsteadiness based on global instability,” *J. Comput. Phys.*, 2007, pp. 924–940.

[23] J. Dandois, “Experimental study of transonic buffet phenomenon on a 3d swept wing,” *J. Physics of Fluids.*, 2016.

[24] L.L. Levy Jr., “Experimental and computational steady and unsteady transonic flows about a thick airfoil,” *J. AIAA*, 1978, pp. 564–572.

[25] C.M. Maksymiuk, T.H. Pulliam, “Viscous transonic airfoil workshop results using ARC2D,” in *Proc. 25th AIAA Aerospace Sciences Meeting*, Reno, NV, 1987.

[26] F. Grossi, M. Braza, Y. Hoarau, “Prediction of transonic buffet by delayed detached eddy simulation,” *J. AIAA*, 2014, pp. 2300–2312.

[27] G. Barakos, D. Drikakis, “Numerical simulation of transonic buffet flows using various turbulence closures,” *Int. J. Heat Fluid Flow*, 2000, pp. 620–626.

[28] G. Barakos, D. Drikakis, “An implicit unfactored method for unsteady turbulent compressible flows with moving boundaries,” *J. Comput. Fluids*, 1999, pp. 899–922.

[29] B.S. Baldwin, H. Lomax, “Thin layer approximation and algebraic model for separated turbulent flows,” in *Proc. 16th AIAA Aerospace Sciences Meeting*, Hunstville, AL, 1978.

[30] P.R. Spalart, S.R. Allmaras, “A one-equation turbulence model for aerodynamic flows,” *J. La Rech. Aerosp.*, 1994.

[31] B.E. Launder, B.I. Sharma, “Application of the energy-dissipation model of turbulence to the calculation of flow near a spinning disc,” *J. Lett. Heat Mass Transf.*, 1974, pp. 131–137.

[32] Y. Nagano, C. Kim, “A two-equation model for heat transport in wall turbulent shear flows,” *J. Heat Transf.*, 1988, pp. 583–589.

[33] D. Sofialidis, P. Prinos, “Development of a non-linear, strain-sensitive k-ω turbulence model,” in *Proc. 11th Symposium on Turbulent Shear Flows*, Grenoble, France, 1997, pp. 89–94.

[34] T.J. Craft, B.E. Launder, K. Suga, “Development and application of a cubic eddyviscosity model of turbulence,” *Int. J. Heat Fluid Flow*, 1996, pp. 108–115.

[35] A. Kourta, G. Petit, J.C. Courty, J.P. Rosenblum, “Buffeting in transonic flow prediction using time-dependent turbulence model,” *Int. J. Numer. Methods Fluids*, 2005, pp. 171–182.

[36] A. Kourta, “Computation of vortex shedding in solid rocket motors using timedependent turbulence model,” *J. Propuls. Power*, 1999, pp. 390–400.

[37] Q. Xiao, H.M. Tsai, F. Liu, “Numerical study of transonic buffet on a supercritical airfoil,” *J. AIAA*, 2006, pp. 620–628.

[38] M.E. Olsen, T.J. Coakley, “The lag model, a turbulence model for non equilibrium flows,” in *Proc. 15th AIAA Computational Fluid Dynamics Conference*, Anaheim, CA, 2001.

[39] R. Carrese, P. Marzocca, O. Levinski, N. Joseph, “Investigation of supercritical airfoil dynamic response due to transonic buffet,” in *Proc. 54th AIAA Aerospace Sciences Meeting*, San Diego, CA, 2016.

[40] N.F. Giannelis, G.A. Vio, “Aeroelastic interactions of a supercritical aerofoil in the presence of transonic shock buffet,” in *Proc. 54th AIAA Aerospace Sciences Meeting*, San Diego, CA, 2016.

[41] G. Alfonsi, "Reynolds-Averaged Navier–Stokes equations for turbulence modeling," *J. Appl. Mech. Rev*, 2009.

[42] H. Schlichting, *Boundary-Layer Theory*, Seventh Edition, McGraw Hill Inc 1979.

[43] G. L. Mellor and H. J. Herring, "A survey of the mean turbulent field closure models," *J. AIAA*, 1973, pp. 590–599.

[44] U. Kutluay, T. Cimen and K. G. Parlak, “A study on controllability of an augmented stability fighter aircraft,” in AIAC Conf., 2017.